Aridification of northwest Australia and nutrient decline in the Timor Sea during the 40 kyr world

Y. Zhang[1], T. Andrade[1†], A. C. Ravelo[1], L. Gong[2], A. Holbourn[2], G. Connock[3*], XL. Liu[3] and I.W. Aiello[4]

[1]Department of Ocean Sciences, University of California, Santa Cruz, CA, USA

[2]Institute of Geosciences, Christian-Albrechts-University, Kiel, Germany

[3]School of Geosciences, University of Oklahoma, Norman, OK, USA

[4]Moss Landing Marine Laboratories, Moss Landing, CA, USA

[†]Blue Planet Systems, Los Gatos, CA, USA

[*]U.S. Geological Survey, Richmond, VA, USA

Corresponding author: Yan Zhang (yzhan543@ucsc.edu)

Key Points:

- Northwest Australia underwent aridification from ~ 1700 to 1400 ka due to restricted Indonesian Throughflow and warm pool contraction.

- Decreased productivity in the Timor Sea from ~ 1700 to 1400 ka reflected decreased nutrient supply from Pacific source water.

- Orbital variation in productivity and terrigenous input in the Timor Sea during the 40 kyr world are driven by multiple mechanisms.

30 **Abstract**

31 Studying tropical hydroclimate and productivity change in the past is critical for understanding
32 global climate dynamics. Northwest Australia is an ideal location for investigating Australian
33 monsoon dynamics, the variability of the Indonesian Throughflow (ITF), and their impact on past
34 productivity and warm pool evolution, which remain poorly understood during the 40 kyr world
35 in the mid-early Pleistocene. In this study, we present multi-proxy records from International
36 Ocean Discovery Program (IODP) Site U1483 in the Timor Sea spanning the last 2000 ka,
37 including orbitally-resolved records from the 40 kyr world between 2000 and 1300 ka. Our results
38 suggest that northwest Australia underwent a step of increased aridification and that productivity
39 in the Timor Sea declined during the transition from ~ 1700 to ~ 1400 ka. We attribute this
40 aridification to the reduced moisture supply to this region caused by the ITF restriction and warm
41 pool contraction. We ascribe the declined productivity to a decrease in the nutrient supply of the
42 Pacific source water associated with global nutrient redistribution. At orbital timescale, multiple
43 mechanisms, including sea level changes, monsoon, and the Intertropical Convergence Zone
44 (ITCZ) dynamics, and variations in the ITF and Walker circulation could control variations of
45 productivity and terrigenous input in the Timor Sea during the 40 kyr world. Our bulk nitrogen
46 and benthic carbon isotope records suggest a strong coupling to biogeochemical changes in the
47 Pacific during this period. This research contributes to a better understanding of tropical
48 hydroclimate and productivity changes during the 40 kyr world.

49 **Plain Language Summary**

50 The northwest Australian region is located at the southwestern edge of the Indo-Pacific Warm Pool
51 and experiences a seasonal monsoon climate. Oceanic and climate conditions in this region are
52 also strongly influenced by the Indonesian Throughflow (ITF), which is the only tropical pathway
53 in the modern ocean connecting the Pacific and Indian Oceans and providing the main conduit for
54 the exchange of water, salt, and heat between these oceans. These conditions make northwest
55 Australia a strategic location to explore Australian monsoon dynamics, the variability of the ITF,
56 and the interaction between tropical hydroclimate and productivity in the past. However, these
57 processes are poorly documented during the 40 kyr world in the mid-early Pleistocene, when
58 glacial-interglacial cycles mainly varied at the 41 kyr obliquity band. Here, we present multiple-
59 proxy marine records from a site directly impacted by the ITF and we examine terrigenous input
60 and productivity changes in this region over the last 2000 kyr. Our results suggest that northwest
61 Australia underwent a step of increased aridification and that productivity in the Timor Sea
62 declined during the transition from ~1700 to ~1400 ka, due to restriction of the ITF, warm pool
63 contraction, and decreased nutrient supply from the Pacific source water.

64 **1 Introduction**

65 Studying past changes in tropical hydroclimate and productivity is recognized as important
66 for understanding global climate dynamics. The northwest Australian region, located at the
67 southern border of the Indo-Pacific Warm Pool (IPWP), is strongly influenced by the trans-
68 equatorial Indonesian Throughflow (ITF) and the seasonal reversal of monsoonal wind and
69 precipitation. It is an ideal location for investigating the variability of the ITF, Australian monsoon
70 dynamics, and their impact on past productivity and IPWP evolution (Beaufort et al., 2010; De
71 Deckker et al., 2014; Holbourn et al., 2005; Müller & Opdyke, 2000). Hydroclimate and
72 productivity changes in the northwest Australian region are influenced by complex, interacting
73 mechanisms. Not only does the Australian monsoon and the seasonal migration of the rain belt

74 (the Intertropical Convergence Zone (ITCZ)) play a prominent role in controlling precipitation and
75 productivity patterns, but this region is also influenced by the tropical Pacific zonal thermal
76 circulation (e.g., Walker circulation), and the regional moisture and nutrient supply regulated by
77 factors such as the intensity of the ITF. Therefore, reconstructions of the terrigenous discharge and
78 productivity variations have the potential to track and elucidate the processes responsible for
79 climatic and oceanographic changes in the northwest Australian region.
80   Global climate has experienced a major transition in the periodicity of the glacial-
81 interglacial cycles from 41 kyr (40 kyr world) to quasi-100 kyr (100 kyr world) during the mid-
82 Pleistocene (Lisiecki & Raymo, 2005; Pisias & Moore, 1981). The vast majority of previous
83 studies on past climate change over the northwest Australian region focused on the Holocene and
84 late Pleistocene (Auer et al., 2019; Beaufort et al., 2010; De Deckker et al., 2014; Holbourn et al.,
85 2005; Ishiwa et al., 2019; Kuhnt et al., 2015; Müller & Opdyke, 2000; Stuut et al., 2014). These
86 studies indicated that insolation forcing and sea level changes have played critical roles in
87 controlling monsoon activity and local productivity in this region during the 100 kyr world
88 (Beaufort et al., 2010; Holbourn et al., 2005; Müller & Opdyke, 2000; Stuut et al., 2014). Several
89 recent reconstructions of sea surface temperature (SST) and terrigenous input along the northwest
90 Australian margin focusing on sediments recovered by International Ocean Discovery Program
91 (IODP) Expedition 356 have offered valuable insight into past ITF and Leeuwin Current variability
92 and the impact on Pliocene and Pleistocene climate (Christensen et al., 2017; He et al., 2021;
93 Petrick et al., 2019; Smith et al., 2020; Stuut et al., 2019). These studies proposed that during the
94 Plio-Pleistocene, increasing near-shore aridity in northwest Australia was largely driven by the
95 progressive constriction of the ITF, resulting in lower SSTs and reduced moisture supply to this
96 region. However, there are few orbitally-resolved reconstructions that directly reflect ITF
97 variability, past productivity changes, and Australian monsoon dynamics during the 40 kyr world
98 in the mid-early Pleistocene (Chen et al., 2022; Zhang et al., 2020).
99   The Timor Sea is located along the main outflow route of the ITF and is therefore strongly
100 influenced by ITF variability and sea level changes. Through regulating the fresh and warm water
101 transport from the Pacific to the Indian Oceans, ITF dynamics interact with monsoon systems and
102 affect the upper ocean thermal structure (Feng et al., 2018) and local productivity of the Timor Sea
103 (Müller & Opdyke, 2000). Holbourn et al. (2005) found that productivity fluctuations in the Timor
104 Sea were strongly influenced by monsoonal wind patterns and were also modulated by sea level–
105 related variations in the intensity of the ITF in the 100 kyr world of the late Pleistocene. Zhang et
106 al. (2020) pointed out that terrigenous/monsoonal discharge in the Timor Sea was linked to Indo-
107 Pacific ITCZ dynamics over the last 410 kyr. In the 100 kyr world, precessional variability in both
108 sea level changes and insolation forcing makes it complicated to differentiate the main driving
109 force of monsoon dynamics and productivity change. However, in the 40 kyr world, sea level and
110 global climate changes are strongly dominated by 41 kyr variability (obliquity band), whereas local
111 insolation forcing is dominated by 19 - 23 kyr variability (precession band). Thus, extending those
112 records to the 40 kyr world will help us disentangle the mechanisms that drive changes in the
113 Australian monsoon, hydroclimate, and productivity in this region.
114   Site U1483, drilled during IODP Expedition 363, is located in the Timor Sea within the
115 main ITF outflow (Figure 1) and thus offers a unique opportunity to investigate ITF dynamics,
116 variations in productivity, and Australian monsoon variability. In this study, using multi-proxy
117 marine records spanning the last 2000 kyr at U1483, including orbitally-resolved records from the
118 40 kyr world between 2000 and 1300 ka, we examine terrigenous input and productivity changes
119 in this region. Firstly, our results suggest that northwest Australia underwent a step of increased

120 aridification and that productivity in the Timor Sea declined from ~ 1700 to ~ 1400 ka, and we
121 discuss possible mechanisms for this transition. Secondly, our high-resolution proxy records from
122 2000 to 1300 ka show orbital variability and we explore the mechanisms that drive this variability.
123 Finally, our bulk nitrogen and benthic carbon isotope records suggest a strong coupling to
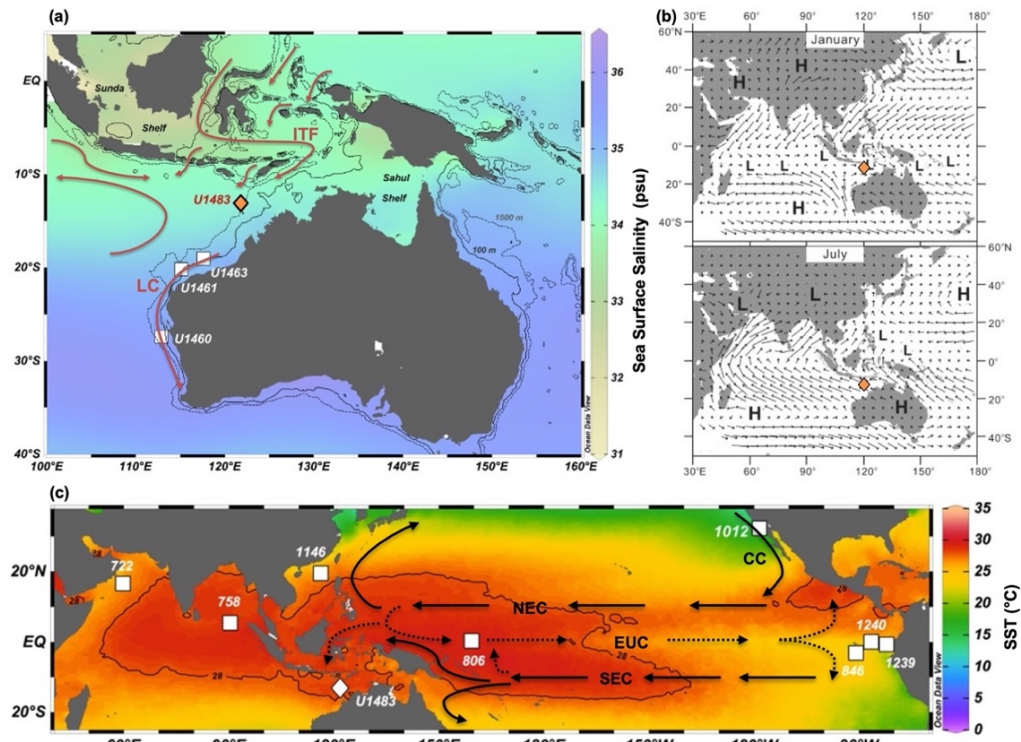124 biogeochemical changes in the Pacific Ocean.

125 **2 Oceanographic and Climatic Setting at Site U1483**

126 Site U1483 was drilled during International Ocean Discovery Program (IODP) Expedition
127 363 in the IPWP. U1483 (13°50.24′S, 121°48.25′E, water depth of 1733m) is located on the Scott
128 Plateau in the Timor Sea in the northeast Indian Ocean off the northwest Australian coast (Figure
129 1), close to Site MD01-2378 (13° 04.95′S,121°47.27′E, water depth of 1783m) (Holbourn et al.,
130 2005). U1483 is located at the southwestern edge of the modern IPWP, beneath the path of the
131 main ITF outflow through the Timor Strait (sill depth of 1500 m) (Figure 1), which is the second
132 largest magnitude component of the ITF in the modern ocean and contributes to the shallow water
133 conditions along the northwest Australian coast (Kuhnt et al., 2004). The ITF brings warm, fresh,
134 and oligotrophic water from the Pacific to the Indian Ocean and affects the upper ocean mixing in
135 the Timor Sea (Feng et al., 2018). Today, hydrographic conditions at Site U1483 are clearly
136 dominated by the ITF outflow of warm, low-salinity surface water.

137 In the modern ocean, the ITF geostrophic transport is strongest in austral winter and is
138 modified by the El Niño-Southern Oscillation (ENSO) through the influence of the Pacific
139 waveguide (Feng et al., 2018). The upper waters of the ITF in the Timor Sea (<1000 m) mostly
140 originate from the subtropical North Pacific surface waters and the North Pacific Intermediate
141 Water, flowing through the Mindanao Current (Gordon & Fine, 1996; Talley & Sprintall, 2005).
142 The intermediate water in the Timor Sea (1000 – 1500 m) is derived from the Antarctic
143 Intermediate Water (AAIW) from the South Pacific via the Halmahera Sea and the deep part of
144 the Indonesian intermediate water (Chen et al., 2022; Tomczak & Godfrey, 1994). The deep water
145 in the Timor Sea is sourced from the Indian Deep water (Tomczak & Godfrey, 1994). The Timor
146 strait has an average depth of around 300 m and since sea level ranged from -100 to +25 m during
147 the mid-early Pleistocene (1300 - 2000 ka) (Rohling et al., 2014), thus there was continuous flow
148 through the Timor passage during the time interval we studied (Figure 1).

149 Northwest Australia experiences monsoon winds, which are directly driven by the
150 temperature and pressure gradient between the land mass and the nearby upper ocean (Suppiah,
151 1992) (Figure 1). During the austral summer, due to the low pressure over the Pilbara, where local
152 insolation heats the land, wind originating from the north-west as a part of south Asian monsoon,
153 brings moisture from the Indian Ocean to northwest Australia, leading to high precipitation and
154 increased riverine sediment load into the ocean (Chang et al., 2006; Suppiah, 1992). During the
155 austral winter, the strong south-east trade winds blow offshore (contributing to the south Asian
156 summer monsoon), resulting in intensified costal upwelling and dry conditions in northwest
157 Australia. Australian monsoon could also be considered as arising from the seasonal migration of
158 the Indo-Pacific ITCZ associated with the tropical overturning (Hadley) circulation changes (Geen
159 et al., 2020; Heidemann et al., 2023), resulting in a distinct seasonal variability in precipitation.
160 Furthermore, northwest Australia is situated to the south of the Maritime continent and borders the
161 IPWP. The precipitation in this region is also affected by the Walker circulation, which is
162 influenced by sea-level modulated land exposure and tropical Pacific dynamics (DiNezio et al.,
163 2016; Heidemann et al., 2023). Thus, reconstructions of terrigenous input and paleo-productivity

164 changes can potentially track past Australian monsoon dynamics and hydroclimate changes over
165 northwest Australia.

166

167
168 **Figure 1.** Study Site U1483 (denoted by the diamond) shown on (a) the map of annual sea surface salinity with
169 regional west Indo-Pacific currents in modern ocean (modified from Gallagher et al. (2009)); (b) on the map of modern
170 Asian-Australian monsoon system (modified from Wang et al. (2005)) and (c) on the map of annual sea surface
171 temperature in tropical Indo-Pacific region (modified from Rousselle et al. (2013). Other sites mentioned in this study
172 are denoted by a square. Panel (b) shows pressure and surface wind pattern in boreal winter (right top panel) and in
173 boreal summer (right bottom panel). Average annual surface temperature and surface salinity from the World Ocean
174 Atlas 2018 (Boyer et al., 2018) plotted using Ocean Data View (ODV) (Schlitzer, 2023). ITF = Indonesian
175 throughflow; LC = Leeuwin Current; NEC = North Equatorial Current; SEC = South Equatorial Current; EUC =
176 Equatorial Undercurrent; CC = California Current.

177 ## 3 Materials and Methods

178 ### 3.1 Site U1483 sedimentology and bulk measurements

179 Cores from U1483 contain clay-rich and clay-foraminifera-rich nannofossil ooze
180 (Rosenthal et al., 2017). Our samples are taken from 0.44 - 199.53 m core composite depth below
181 seafloor (CCSF), which is above the first appearance of soft sediment deformation. We sampled
182 every 150 cm to achieve an average ~ 15 kyr resolution spanning from ~ 2000 to 0 ka and every
183 30 cm to achieve an average ~ 3 kyr resolution between 127.05 - 199.53 m CCSF spanning from
184 ~ 2000 to ~ 1300 ka. Bulk nitrogen isotope (δ^{15}N) and total nitrogen (TN, wt%) were analyzed
185 from these samples (methods see Text S1). A subset of the samples spanning from ~ 2000 to 0 ka
186 with an average ~ 22 ka resolution were analyzed for carbon isotope of total organic carbon (TOC)
187 ($\delta^{13}C_{org}$) to distinguish the terrestrial and marine sourced organic matter (methods see Text S2).
188 TOC:TN ratios are calculated to help assess inorganic N contamination. All bulk sediment
189 measurements were analyzed on the Carlo Erba 1108 elemental analyzer (interfaced to a Thermo

190 Finningan Delta Plus XP IRMS) at the University of California, Santa Cruz. The external precision
191 is $\pm$ 0.20 ‰ for $\delta^{15}N$, $\pm$ 0.10 wt% for TN wt%, $\pm$ 0.10‰ for $\delta^{13}C_{org}$ and $\pm$ 0.10 for TOC:TN ratios.
192 We obtained $CaCO_3$ wt% using three methods (Text S3, Figures S1 & S2). Our results confirm
193 that the estimations of $CaCO_3$ wt% $_{EA}$ are accurate and thus we use $CaCO_3$ wt% $_{EA}$ values for all
194 the paleoceanographic interpretations hereafter in this paper.

3.2 Benthic foraminiferal stable isotope analysis and age model

196 Benthic foraminiferal stable isotope measurements (from 1922 to 1589 ka) were conducted
197 at the Institute of Geosciences, Christian-Albrechts-University, Kiel (Germany). Detailed methods
198 are provided in Gong et al. (2023). The analysis was carried out on the benthic foraminifers
199 *Cibicidoides wuellerstorfi and/or Cibicidoides mundulus* from the size fraction >250 μm.
200 *Uvigerina* spp. were measured when *C. wuellerstorfi* and *C. mundulus* were rare or absent (Table
201 S2). The external standard error is better than $\pm$ 0.08‰ for $\delta^{18}O$ and $\pm$ 0.05‰ for $\delta^{13}C$ based on
202 international standards.
203 From 1922 to 0 ka, our age model is based on tuning the benthic foraminiferal $\delta^{18}O$ to the
204 LR04 stack (Lisiecki & Raymo, 2005), using published data from Zhang et al., (2020) (420 - 0 ka)
205 and from Gong et al. (2023) (1587 - 420 ka) and data from this study (1922 - 1587 ka) (Figure S3);
206 from 2000 to 1922 ka, our age model is generated by correlating XRF-derived high-resolution
207 records of Log (Mn/S) (see section 3.3) from Site U1483 and the LR04 stack using QAnalySeries
208 (Kotov & Pälike, 2018) using 5 tie points (Figure S4). Mass-based accumulation rates (MAR) are
209 calculated based on the sedimentation rates and dry bulk density (DBD) values (Figure S5).

3.3 Other analyses

211 32 sediment samples were selected for lipid biomarker analysis using a recently developed
212 reverse phase liquid chromatography quadrupole time-of-flight mass spectrometry method with
213 electrospray ionization (RPLC-ESI-qTOF-MS) and were measured in University of Oklahoma.
214 Sample preparation and instrument setup followed method published in Connock et al. (2022). The
215 Prahl & Wakeham (1987) calibration was applied to the $U_{37}^{K\prime}$ - based SST, which exhibits same
216 features and trend as using Müller et al., (1998) calibration (Table S2). The Schouten et al. (2002)
217 calibration was applied to the TEX_{86} - based SST record. The Branched versus Isoprenoid
218 Tetraether (BIT) index was calculated following Hopmans et al. (2004), as an indication of soil
219 inputs (thus terrigenous input) of glycerol dialkyl glycerol tetraether (GDGT) (Hopmans et al.,
220 2004). We performed high-resolution X-ray fluorescence (XRF) core scanning with the 2nd
221 Generation Avaatech XRF Core Scanner at the Institute of Geosciences, Christian-Albrechts-
222 University, Kiel (Germany). The archive halves were equilibrated to room temperature before
223 scanning and a thin layer of sediment was removed from the top to obtain a fresh, even surface for
224 scanning. We scanned at 2 cm intervals along the shipboard splice with approximately 1–2 m
225 overlaps at splice tie points. Scanning was performed with 10 kV (750 μA, 10s acquisition time,
226 no filter) and 30 kV (2000 μA, 20s acquisition time, Pd-thick filter) on the archive halves, which
227 were covered with a 4 μm thick Chemplex Prolene Thin-Film foil to prevent contamination of the
228 XRF detector. We used a crosscore slit size of 1.2 cm and a downcore slit size of 1 cm. The data
229 reported here were acquired by a XR-100CR detector from Amptek and an Oxford Instruments
230 50W XTF5011 X-Ray tube with rhodium (Rh) target material. Raw X-ray spectra were converted
231 into area counts using the iterative least-square software package WIN_AXIL from Canberra
232 Eurisys and a core-specific model. The elements Al, Si, S, K, Ca, Ti, Mn, and Fe were analyzed
233 with the 10-kV setting. Measured area counts per second of the spectral peaks of each element

234 were transferred to logarithmic elemental ratios, which provide the most easily interpretable
235 signals of relative changes in chemical composition. The use of elemental ratios minimizes the
236 risk of measurement artifacts from variable signal intensities due to changes in sediment density,
237 pore volume, water content and matrix effects. We obtained the in-situ visible light reflectance
238 spectroscopy data from the LIMS Online Report Portal. Following Gong et al., (2023), the relative
239 absorption band depth at 660 nm was calculated using the algorithm of Rein and Sirocko (2002)
240 (Text S4). Measurements for uranium (U, ppm) and potassium (K, wt%) were deconvolved from
241 Natural Gamma Radiation (NGR) data generated on IODP Expedition 363 (De Vleeschouwer
242 2017; Rosenthal, 2018). Correlation matrix analyses and T-test were made by excel data analysis
243 among different proxies. Spectral and cross-spectral analyses were performed using Analyseries
244 (Paillard et al., 1996). Wavelet coherence analysis was performed using biwavelet package in R.

4 Results

246   The data set generated in this study reveals two main features: **1)** a long-term climate
247 transition over the last 2000 kyr (section 4.1) and **2)** orbitally-paced variations during the 40 kyr
248 world, from ~ 2000 to ~ 1300 ka (section 4.2). In summary, a marked transition occurred in the
249 productivity and terrigenous input records from ~ 1700 to ~ 1400 ka, with both productivity and
250 terrigenous input records shifting to lower values after the transition. At orbital timescale, our
251 results suggest that the variability of the productivity records occurs with a different dominant
252 periodicity from that of terrigenous input during the 40 kyr world.

4.1 Long-term transition from ~ 1700 to ~ 1400 ka

4.1.1 Terrigenous input records

255   At Site U1483, the terrigenous input is mainly from the riverine run-off from the northwest
256 Australian region (e.g., the Fitzroy and Ord Rivers), rather than from the South Indonesian
257 archipelago, and includes little aeolian dust (Gingele & De Deckker, 2004; Kuhnt et al., 2015;
258 Stuut et al., 2014; Zhang et al., 2020). In this study, K wt% (MAR) and Log $((Al+K+Ti+Fe)/Ca)$
259 are used as indicators of the terrigenous input at U1483. K wt% has been used previously as a
260 proxy for riverine runoff and continental moisture in northwest Australian regions because clays
261 and feldspars contain K-bearing aluminosilicates (Christensen et al., 2017; Ehrenberg & Svånå,
262 2001). Following Gong et al. (2023), the sum of elements aluminum (Al), potassium (K), iron (Fe)
263 and titanium (Ti) (as proxies for the terrigenous derived sediment) normalized against calcium
264 (Ca) (derived from marine biogenic carbonate), Log $((Al+K+Ti+Fe)/Ca)$, is also used as a proxy
265 of terrigenous input in this study.
266   Over the last 2000 kyr, a long-term transition is evident between ~ 1700 and ~ 1400 ka in
267 both terrigenous input records, after which the terrigenous input shifts to generally lower values
268 (Figure 2). From ~ 2000 to ~ 1300 ka, the Log $((Al+K+Ti+Fe)/Ca)$ values are significantly
269 positively correlated with K wt% (Figure 3, $R^2 = 0.76$, $p<0.001$), indicating that K wt% is not a
270 result of dilution effects. $CaCO_3$ wt% $_{EA}$ values are significantly negatively correlated with K wt%
271 from ~ 2000 to ~ 1300 ka (Figure 3, $R^2= 0.66$, $p<0.001$). According to the shipboard core
272 description almost all the $CaCO_3$ in the sediment relates to marine primary productivity (without
273 terrigenous or authigenic source) at U1483 (Rosenthal et al., 2018). The water depth of U1483 is
274 1733 m, which was above the lysocline during the mid-early Pleistocene; thus, the effects of
275 dissolution are minimal. At U1483, the high coherence among Log $((Al+K+Ti+Fe)/Ca)$, K wt%
276 and $CaCO_3$ wt% $_{EA}$ (Figure 3, Tables 2 & 3) indicates that changes in the $CaCO_3$ wt% $_{EA}$ is a result

277   of varying amounts of dilution, low amounts of $CaCO_3$ implying high dilution of the sediment
278   from terrigenous flux. Thus, K wt%, CaCO3 wt% $_{EA}$ and Log $((Al+K+Ti+Fe)/Ca)$ are used as
279   indicators for terrigenous input. A striking shift occurred at $\sim$ 1640 ka in all three proxy records
280   (Figure 3), when $CaCO_3$ wt% $_{EA}$ increased from 35% to 70%, K wt% decreased from 1.7% to 0.9%
281   and Log $((Al+K+Ti+Fe)/Ca)$ decreased from -0.32 to -1.08, indicating a rapid decrease in
282   terrigenous input within $\sim$ 10 kyrs. T-test reveals that all terrigenous input proxies exhibit
283   significant changes ($p<0.0001$) in their averages before and after 1625 ka, indicating lower
284   terrigenous input between 1625 to 1300 ka (Table 1).

285   **4.1.2   Productivity records**

286   We use TN wt% (MAR) and $RABD_{660}$ as productivity proxies and use U and Log (Mn/S)
287   as indicators for bottom water oxygen variations. The flux of TN (TN MAR) is calculated from
288   the TN wt% and it reflects the primary production in the surface water. $RABD_{660}$ is derived from
289   the visible light reflectance spectroscopy reflecting the chlorins concentration, which is reported
290   to be highly correlated to marine organic carbon content and marine primary productivity (Harris
291   et al., 1996; Rein & Sirocko, 2002), and can be used as a productivity indicator. Following Gong
292   et al. (2023), we use the logarithmic ratios of the redox-sensitive elements manganese (Mn) and
293   sulfur (S) (Log (Mn/S)) as proxies for bottom water oxygenation, with higher Log (Mn/S)
294   corresponding to oxygenated environments. The concentration of authigenic U could reflect
295   bottom-water redox conditions because U precipitates in anoxic environments due to its
296   insolubility (Klinkhammer & Palmer, 1991). As nutrients are supplied to the surface by upwelling
297   and organic matter is exported to the sea floor, the consumption of dissolved oxygen in the upper
298   ocean increases, leading to anoxic environments and U precipitation in bottom waters. Thus, the
299   concentration of U in the sediment is expected to be positively correlated to productivity. Since
300    $CaCO_3$ in sediment at U1483 is marine-derived, the flux of $CaCO_3$ ($CaCO_3$ MAR) reflects the bio-
301   carbonate productivity in this region.

302   Over the last 2000 kyr, productivity (inferred by TN MAR) shifted to lower values from $\sim$
303   1700 to $\sim$ 1400 ka (Figure 2). We note that $CaCO_3$ MAR exhibits a different behavior to TN MAR,
304   which increased first during 1650 - 1600 ka, while TN MAR started to decrease. Between 2000
305   and 1300 ka, TN wt%, $RABD_{660}$, Log (Mn/S) and U are significantly strongly correlated with each
306   other (Figure 3, Tables 2 & 3, $p<0.001$). The striking shift at $\sim$ 1650 ka, which appeared in the
307   productivity records (inferred by TN wt% and $RABD_{660}$), is not pronounced in the bottom water
308   oxygen records (inferred by U and log (Mn/S)), during which productivity decreased rapidly
309   within $\sim$10 kyrs (Figure 3). T-test reveals that productivity and oxygen proxies show significant
310   changes ($p<0.0001$) in their averages before and after 1625 ka, indicating a shift to lower
311   productivity and higher bottom water oxygen from 1625 to 1300 ka (Table 1). Oxygen (2000 –
312   1300 ka) and productivity (typically after 1650 ka) records show rhythmic variations during
313   glacial-interglacial cycles, with higher TN MAR/U/$RABD_{660}$ and lower Log (Mn/S) values during
314   glacial intervals, indicating high productivity during colder times (Figure 3).

315   **4.1.3   SST and Biomarkers**

316        $U^{K\prime}_{37}$ values of the 32 selected samples analyzed range from 0.77 to 0.99 and TEX_{86} values
317   range from 0.65 to 0.73. We obtained estimates of 22.6°C to 29.2°C based on $U^{K\prime}_{37}$ index using the
318   Prahl & Wakeham (1987) calibration (Figure 3) and of 26.5°C to 29.9°C based on TEX_{86} index
319   using the Schouten et al. (2002) calibration (Figure S6). The $U^{K\prime}_{37}$ record generally agrees with the
320   TEX_{86} record but larger SST decreases occur in the $U^{K\prime}_{37}$ record ($\sim$ 29°C to 22°C) compared to the

321 TEX$_{86}$ record ($\sim$ 28°C to 25°C) during the 1650 ka shift (Figure S6). C$_{37}$ total (ng g sed^{-1}) is
322 consistent with TN wt% (and other productivity records) and captures glacial-interglacial
323 variability (Figure S6). Relatively low SST corresponds to relatively high productivity. The BIT
324 index shows a decreasing trend from 2000 to $\sim$ 1450 ka, with a range between 0.09 and 0.18 and
325 an average value of 0.14 (BIT < 0.2; Figure S6). The 1650 ka shift in the BIT values corresponds
326 to a minimum value of 0.09. Over the last 2000 ka, there is no pronounced secular trend or long-
327 term transition observed in our low-resolution SST records (Figure 3); the intense cooling event
328 occurring at 1650 ka likely corresponds to the 1650 ka shift in the productivity record (Figures 3
329 and S6).

4.1.4 Bulk nitrogen isotopes

331 To distinguish between terrigenous and marine derived organic matter at U1483, we
332 measured $\delta^{13}C_{org}$ and calculated TOC:TN ratios over the last 2000 ka. Both TOC:TN (average =
333 11.03) and $\delta^{13}C_{org}$ values (average = -20.16‰) are within the typical range of marine organic
334 matter (Meyers, 1994). $\delta^{13}C_{org}$ ranges between -18.67‰ to -20.54‰ with no systemic variation
335 and shows relatively constant values fluctuated around -20‰ (Figure S7). No correlation is shown
336 between $\delta^{13}C_{org}$ and TOC/TN (R^2 = 0.01, p< 0.001) and between bulk $\delta^{15}N$ and $\delta^{13}C_{org}$ (R^2 = 0.09,
337 P = 0.7) (Figure S7). These results suggest that the organic matter at U1483 is primarily of marine
338 origin with minimal or little terrestrial influence, which is supported by the low BIT index (<0.2)
339 (Figure S6), which is consistent with Holbourn et al. (2005) and Zhang et al. (2020). A significant
340 positive linear correlation between TN wt% and TOC wt% (R^2 = 0.74, p < 0.001) with a y-intercept
341 of 0.04 suggests minimal contribution from inorganic N (Figure S7). No correlation (R^2 = 0.09, p
342 < 0.001) between bulk $\delta^{15}N$ versus TN wt% indicates minor alteration from early diagenesis on
343 original $\delta^{15}N$ values (Figure S8).
344 Over the last 2000 kyr, bulk $\delta^{15}N$ at U1483 ranges between 4.2‰ and 8.1‰ (average =
345 6.2‰) and exhibits no pronounced secular trend (Figure 2). From 2000 to 1300 ka, there is no
346 significant change in the average value of $\delta^{15}N$ before and after 1625 ka (Table 1). From 2000 to
347 1625 ka, bulk $\delta^{15}N$ is negatively correlated to TN wt% (R^2= 0.47, P < 0.001) and U (R^2= 0.12, P
348 < 0.001), and positively correlated to Log (Mn/S) (R^2= 0.23, P < 0.001). From 1625 to 1300 ka,
349 bulk $\delta^{15}N$ is not correlated to TN wt% (R^2= 0.00, P = 0.9) and to oxygen proxies. Bulk $\delta^{15}N$ shows
350 little correlation to any other proxies (Table 2 & 3).

4.1.5 Benthic foraminiferal carbon isotopes

352 Benthic foraminiferal $\delta^{13}C$ at U1483 ranges between - 0.74‰ – 0.51‰ from 2000 to 1300
353 ka and there is no significant change in average value before and after $\sim$ 1625 ka (Figure 3 and
354 Table 1), as for the bulk $\delta^{15}N$ records. Benthic $\delta^{13}C$ does not exhibit a pronounced long-term
355 secular trend but shows a strong negative correlation with U values (Figures 3 and S9). Benthic
356 $\delta^{13}C$ shows rhythmic variations following glacial-interglacial cycles after $\sim$ 1650 ka, with high
357 $\delta^{13}C$ values during interglacial periods and low $\delta^{13}C$ values during glacial periods.

4.2 Orbital Variability

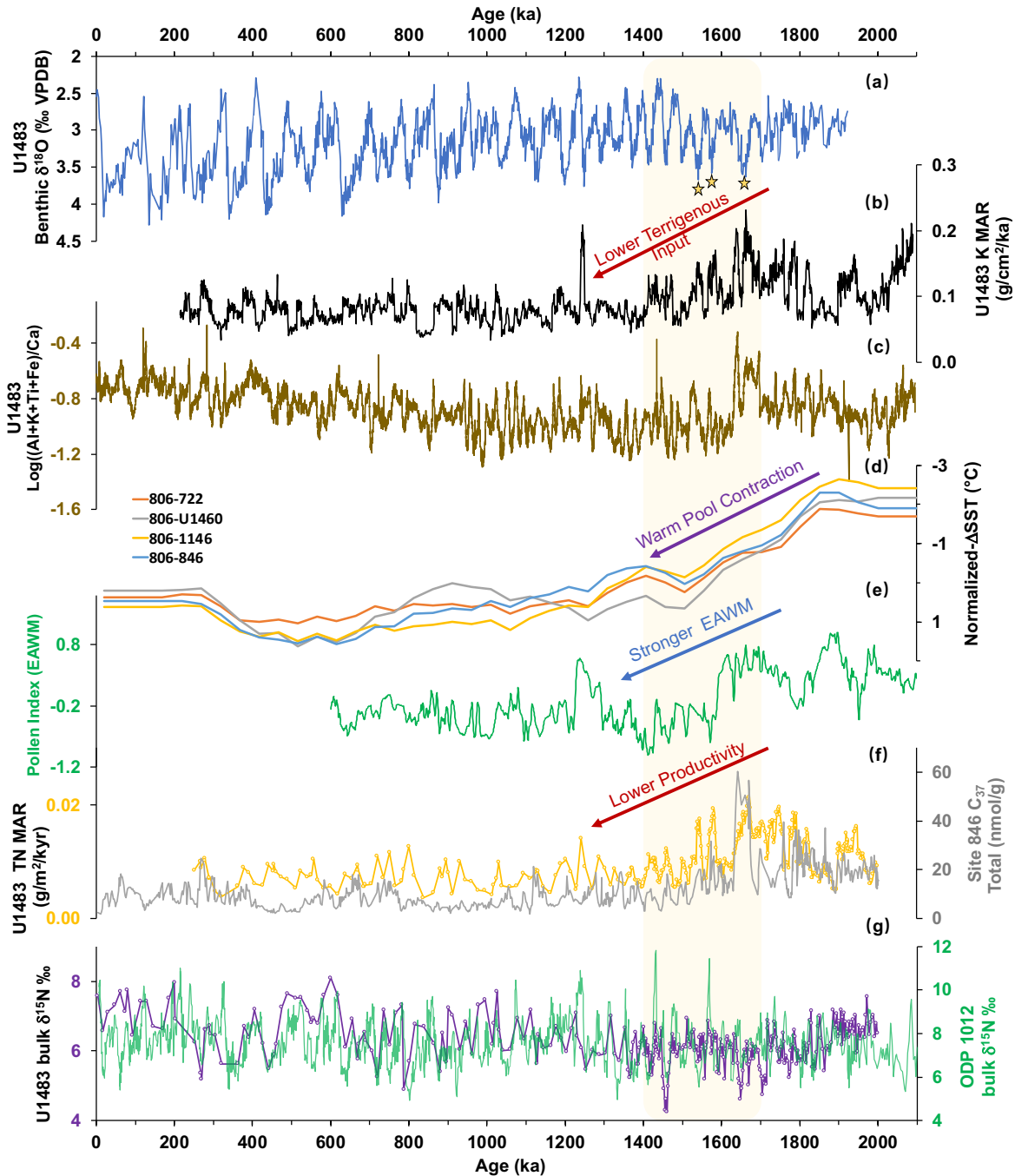### 4.2.1 Spectral analysis

360 Due to the appearance of the striking shift at $\sim$ 1640 - 1650 ka, the records are divided into
361 two parts (before and after 1625 ka), and spectral analysis was performed on each of the time
362 intervals (Figures 4 and S10). Spectral analyses reveal that variance in the terrigenous input records
363 (inferred by Log ((Al+K+Ti+Fe)/Ca) and K wt%) is dominated by the 19 - 23 kyr (precession)

364 periodicities throughout the period 2000 - 1300 ka and 41 kyr (obliquity) periodicity occurred only
365 after 1625 ka. Productivity (inferred by TN wt%), bottom water oxygen (inferred by Log (Mn/S)
366 and U) and benthic δ^{13}C show similar spectral characteristics to that of benthic δ^{18}O. They show
367 variability concentrated in the precession band before 1625 ka followed by pronounced obliquity
368 variability after 1625 ka. Bulk δ^{15}N variability is concentrated in the precession band throughout
369 the period 2000 - 1300 ka with dominant obliquity variability occurring only after 1625 ka.
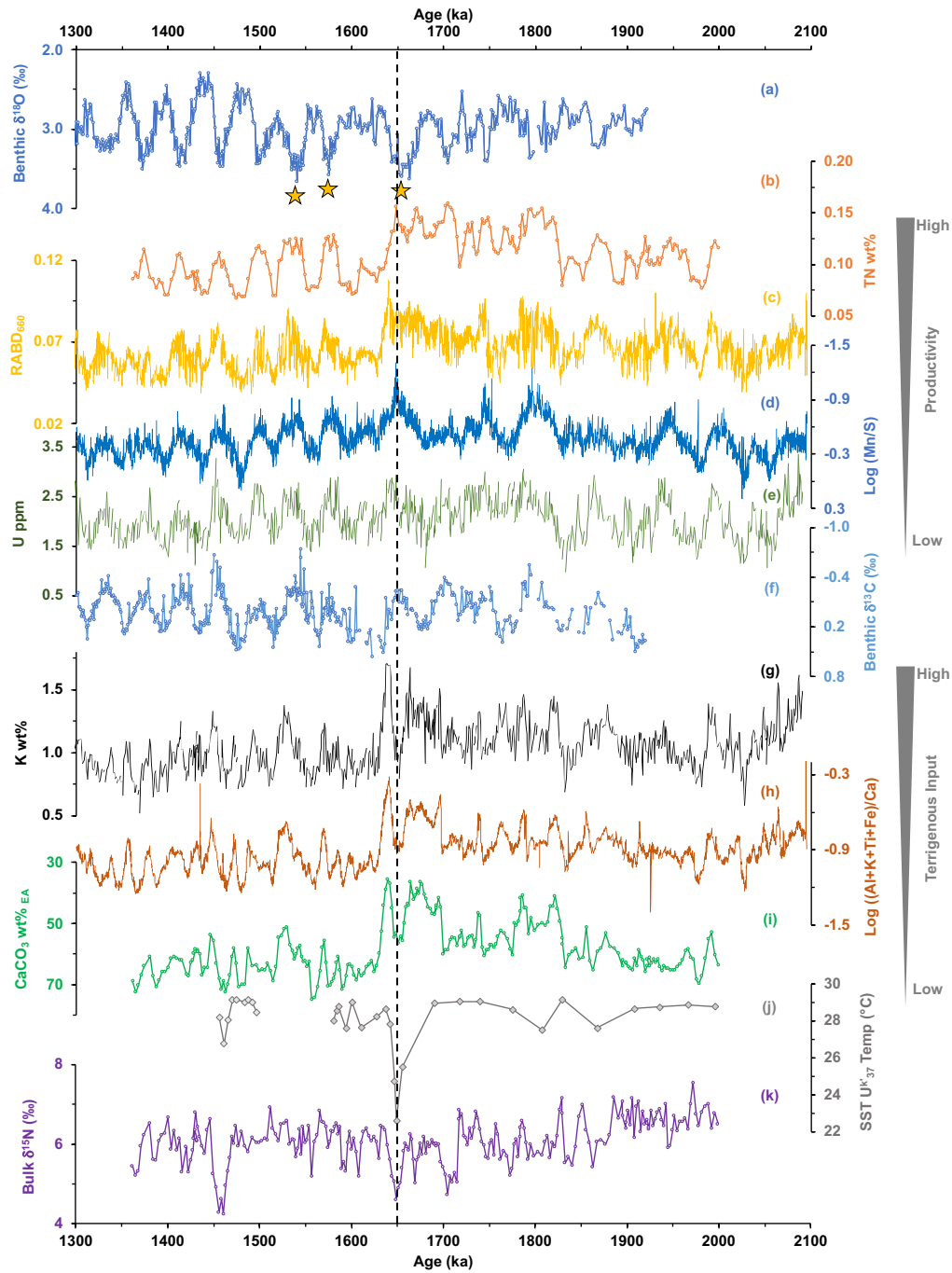
370 **4.2.2   Cross-spectral analysis and phase relationships**

371 Wavelet coherence analysis was performed (Figure 5) and phase relationships were
372 summarized (Figure 6). Productivity (inferred by TN wt%), bottom water oxygen (inferred by Log
373 (Mn/S) and U) and benthic δ^{13}C exhibit similar behaviors to that of benthic δ^{18}O, showing high
374 coherency (>0.8) with obliquity from ~1600 to 1300 ka and some coherency with precession
375 between ~ 1900 and 1700 ka. Terrigenous input (inferred by (Log ((Al+K+Ti+Fe)/Ca) and K
376 wt%)) shows high coherency (>0.8) with precession from ~ 1550 to 1300 ka. Bulk δ^{15}N exhibits
377 intermittent high coherency with precession through 2000 - 1300 ka and with obliquity only
378 between ~ 1500 and 1350 ka. Besides being strongly coherent to benthic δ^{18}O, benthic δ^{13}C
379 exhibits high coherence (>0.8) with U ppm at the obliquity band from 2000 to 1300 ka and are out
380 of phase with each other (with relatively high δ^{13}C values corresponding to relatively low U
381 values).
382

Figure 2. Long - term records generated at Site U1483 from this study are plotted with other related records over the last 2000 kyr. (a) Benthic foraminiferal $\delta^{18}O$ from Site U1483 indicates global ice volume change and yellow stars indicate enhanced glaciations from 1700 to 1500 ka. Terrigenous input records from U1483 are inferred by K MAR (b) and Log ((Al+K+Ti+Fe)/Ca) (c). (d) Normalized ΔSST gradient in the IPWP is calculated by subtracting the SST records of Sites 722, U1460, 1146, 846 from central IPWP Site 806. See original SST records and site map in supplementary Figure S13. (e) East Asian winter monsoon record is inferred by pollen index, data from Xin et al., (2020). (f) The productivity record (inferred by TN MAR) from U1483 is plotted with the productivity record based on C_{37} total (ng g sed^{-1}) from east equatorial Pacific Site 846, data from Lawrence et al., (2006). (g) Bulk $\delta^{15}N$ from U1483 is plotted with that from California margin Site 1012, data from Liu et al., (2008). The yellow bar indicates the transition period from 1700 to 1400 ka.

395

396
397 **Figure 3.** Orbitally-resolved records generated at Site U1483 over the interval ~ 2000 to 1300 ka. Benthic
398 foraminiferal $\delta^{18}O$ (a) is plotted as chronological reference and yellow stars indicate enhanced glaciations from 1700
399 to 1500 ka. Productivity changes expressed as TN wt% (b) and RABD$_{660}$ (c); bottom water oxygen expressed as Log
400 (Mn/S) (d) and U ppm (e). Benthic foraminiferal $\delta^{13}C$ (f) U. Terrigenous input changes are expressed by K wt% (g),
401 Log((Al+K+Ti+Fe)/Ca) (h) and CaCO$_3$ wt% $_{EA}$ (i). Low resolution SST (j) based on $U^{K'}_{37}$ index using the Prahl &
402 Wakeham (1987) calibration and bulk $\delta^{15}N$ (k). Orbitally-resolved records show significant correlation with each other
403 (Tables 2 & 3); filtered records are shown in supplementary Figures S14 and S15. The black dash line indicates the
404 unusual rapid event at ~ 1650 ka.
405

5   Discussion

5.1 The 1700 - 1400 ka transition in terrigenous input

As terrigenous input at U1483 is primarily from riverine sources of the northwest Australian region, the shift to lower terrigenous input from ~ 1700 to ~ 1400 ka (Figure 2) could be a result of **1)** a final step in the aridification of northwest Australia and consequently less riverine input to the ocean due to decreased precipitation; or **2)** a transition to a wet climate and enhanced vegetation cover in this region resulting in less riverine sediment load. Most available Australian paleoclimate records monitor central and southeast Australian conditions (Christensen et al., 2017; Kershaw et al., 2017; Martin, 2006); few records are from coastal northwest Australia, and there are no published records extending to the mid-early Pleistocene (40 kyr world), the time period of this study. In northwest Australia, a transition to an arid landscape was inferred by the replacement of the casuarinaceous forests with grasslands by the late Pleistocene (Martin & McMinn, 1994), but these studies do not cover the 1700 – 1400 ka interval. Although there are no continental paleoclimate studies from northwest Australia that span the same time interval as our study, evidence from other regions of Australia strongly suggests increasing aridity during the Pleistocene (Christensen et al., 2017 and references therein; Kershaw et al., 2003a). Firstly, an overall decreasing trend of precipitation in Australia through the Pleistocene has been proposed (Martin, 2006). Secondly, an enhanced aridification at ~ 1500 ka at Lake Bungunniain in southern Australia (McLaren et al., 2012) and a transition to aridity possibly at 1600 ka at Lake Amadeus in the central Australia have been reported (Chen & Barton, 1991). Therefore, all the evidence points to increasing aridity and reduced runoff, rather than a shift to a wetter continental northwest Australia, as the most likely explanation for a decrease in terrigenous input from 1700 to 1400 ka in our records (Figure 2). This is consistent with the interpretative framework used by Christensen et al., (2017) that K wt% can be used as a continental moisture proxy, with low K wt% corresponding to drier conditions and vice versa. This is also consistent with other previous palaeoceanographic studies, which indicate that increasing aridity off the northwest Australian coast from ~ 1700 to ~ 1400 ka corresponds to reduced ITF inferred from cooling SSTs (He et al., 2021; Petrick et al., 2019; Smith et al., 2020).

The rainfall pattern in northwest Australia could be influenced by three main processes. **1)** The dynamics of the Australian summer monsoon may play a major role since about three quarters of the rainfall in northern Australia is registered during the monsoon season in western Australia atpresent (Chang et al., 2006; Suppiah, 1992). **2)** The strength of the ITF, which brings heat and moisture from the equatorial Pacific, can influence the land-sea temperature gradient and precipitation patterns in northwest Australia (Christensen et al., 2017; Ishiwa et al., 2019). Model results and long-term geological records have shown that the restriction of the ITF would lead to a significant reduction of rainfall in Australia and contribute to its aridity (Christensen et al., 2017; Stuut et al., 2019). **3)** The large-scale tropical hydroclimate, including the thermal evolution of the IPWP and Walker circulation dynamics, can impact the Australian climate. Walker circulation is known to play a predominant role in hydroclimate changes in the equatorial Indo-Pacific region (through modifying ENSO events) and is closely linked to SST pattern across the Pacific (Dang et al., 2020; Kaboth-Bahr & Mudelsee, 2022). In sum, the shift to lower terrigenous input during 1700 - 1400 ka, indicating a major step of aridification in the northwest Australian region, could be a result of **1)** a reduction in the strength of the Australian summer monsoon; **2)** a reduction of the intensity of the ITF; **3)** a shift in the thermal evolution of the warm pool and Walker circulation. These three possibilities are discussed below, although it is worth pointing out that the monsoon

451 systems, the ITF, and Walker circulation interact with each other, and these mechanisms are not
452 necessarily mutually exclusive.

5.1.1   Shift in the Asian-Australian monsoon system

454 The first possible candidate causing the 1700 - 1400 ka transition in the precipitation in
455 northwest Australia is a shift in the monsoon system. The East Asian winter monsoon (EAWM) is
456 related to the Siberian high and is primarily driven by the high latitude forcing in the North
457 Hemisphere (NH); the strong cold winds could flow across the equator and influence the summer
458 monsoon and hydroclimate in the South Hemisphere (SH) (Liu et al., 2015). In this context, we
459 expect that the Australian summer monsoon correlates to the EAWM which can be tracked by
460 EAWM paleoclimate records. An intensification of the EAWM at ~ 1600 ka has been widely
461 documented in loess and pollen records (Ding et al., 2002; Sun et al., 2006, 2019; Xin et al., 2020)
462 and has been associated with a global climate cooling trend (Xin et al., 2020). The timing of the
463 intensification in the EAWM (inferred by the pollen index) roughly occurs during the transition to
464 drier conditions in northwest Australia inferred from the terrigenous input record at U1483 (Figure
465 2). This is the opposite of what we would expect if the observed decrease in terrigenous input was
466 primarily driven by the coupling of the Australian summer monsoon to changes in the strength of
467 the EAWM. Therefore, we conclude that the shift in the monsoon systems did not directly drive
468 the long-term transition observed in our terrigenous input records but could contribute to it in a
469 complicated way through the interactions with the ITF (see section 5.1.3 below).

5.1.2   Shift in the strength of the ITF

471 The second possible explanation for changes in precipitation in northwest Australia from
472 ~ 1700 to ~ 1400 ka is the restriction of the ITF. The restriction of the ITF has been implicated in
473 previous studies as the cause of intense cooling and aridification sometime between 1700 ka and
474 1500 ka at northwest/west Australian sites (U1460, U1461, U1463) (Christensen et al., 2017; He
475 et al., 2021; Petrick et al., 2019; Smith et al., 2020). Consistent with these other studies, our records
476 at U1483 not only show a similar transition in terrigenous input (Figure S11) but also exhibit the
477 intense surface cooling event (Figure S12) at ~ 1650 ka contemporaneous with relatively low
478 terrigenous input (Figure 3). Previous studies attributed the surface cooling events to a weakening
479 of the ITF driven by global sea level changes and ongoing tectonic activities (Petrick et al., 2019)
480 and proposed that increasing northwest Australian aridity was driven by the progressive
481 constriction of the ITF during the Plio-Pleistocene, which resulted in lower SSTs and reduced
482 moisture reaching this region (Christensen et al., 2017; Smith et al., 2020). Site U1483 is directly
483 influenced by the ITF and, compared to other sites studied, better located to track changes in the
484 ITF. The ITF transport is determined by the surface pressure gradient between the Pacific and
485 Indian Ocean, which is influenced by changes in sea level, wind-forcing (e.g., the strength of the
486 East Asian monsoon) and buoyancy forcing (Feng et al., 2018). Based on the records at U1483,
487 we discuss two plausible mechanisms responsible for the restriction of the ITF from ~1700 to ~
488 1500 ka; one mechanism is related to the effects of sea level change and the other to Asian
489 monsoon-related circulation.

490 Sea level changes are thought to drive the flow in the Timor passage on glacial/deglacial
491 timescales during the Holocene and Pleistocene (Kuhnt et al., 2004). From ~ 1700 to ~ 1500 ka,
492 the benthic $\delta^{18}O$ record show enhanced glaciations (Figure 2), indicating decreasing glacial sea
493 levels, which would contribute to restriction of the ITF and reduce moisture supply and
494 precipitation of the northwest Australian region. Specifically, the observed intense cooling event
495 at ~ 1650 ka occurs during the first enhanced glaciation (MIS 58) (Figure 3), consistent with the

496 strong coupling between the surface cooling and the reduction of the ITF proposed in previous
497 studies (He et al., 2021; Petrick et al., 2019; Smith et al., 2020). In addition, sea level
498 reconstructions based on measurements and simulations show decreasing glacial sea levels
499 changing from -50 to -85 m from ~ 1700 to ~ 1500 ka (Berends et al., 2021 and references therein),
500 supporting the idea that global sea level change contributed to the reduction of the ITF and the
501 aridity of northwest Australia during this period.
502 Changes in the strength of the Asian monsoon system could also affect the intensity of the
503 ITF; thus, it is important to consider how the ITF was impacted during the transition in the strength
504 of the EAWM from ~ 1700 to ~ 1500 ka (see section 5.1.1). In the modern ocean, the strength of
505 the ITF varies seasonally responding to the wind forcing (Kuhnt et al., 2004) and the important
506 negative feedback between the Asian monsoon and the intensity of the ITF has been proposed
507 (Gordon et al., 2003). During the boreal winter (Australian summer), the northwesterly Asian
508 monsoon drives buoyant, low-salinity Java Sea surface water into the southern Makassar Strait,
509 creating a northward pressure gradient in the surface layer, which inhibits the overall strength of
510 the ITF, cooling the east Indian Ocean and strengthening the Asian winter monsoon (Gordon et
511 al., 2003). In this context, the intensification of the EAWM at ~ 1600 ka may have weakened the
512 ITF and contributed to increase aridity in northwest Australia. Moreover, the ongoing tectonic
513 activity in the Indonesian archipelago through the Pleistocene could also potentially contribute to
514 the weakening of the ITF during this time (Petrick et al., 2019 and references therein).
515 In summary, lower glacial sea levels, negative Asian monsoon-ITF feedbacks and potential
516 tectonic changes through the Pleistocene could result in significant restriction of the ITF from ~
517 1700 to ~ 1400 ka and contribute to the increased aridity of northwest Australia after the transition.

518 ### 5.1.3 Shift in the Walker circulation and warm pool contraction

519 The third possible mechanism for changes in precipitation in northwest Australia from ~
520 1700 to ~ 1400 ka is related to the Walker circulation and evolution of the IPWP, which are thought
521 to be important drivers of the hydrological cycle in the Indo-Pacific region (e.g., Brierley et al.,
522 2009; Hollstein et al., 2018). Several studies found that the modern pattern of east–west SST
523 asymmetry in the tropical Pacific, was not established until at ~ 1600 - 1500 ka (Berner et al.,
524 2022; Kaboth-Bahr & Mudelsee, 2022; Lawrence et al., 2006; Wara et al., 2005; Ravelo et al.,
525 2006), indicating a steplike intensification in the Walker circulation during this time. It has been
526 reported that that the increasing zonal SST gradient across the equatorial Pacific is tightly linked
527 to increasing meridional SST gradient via the wind-driven circulation and upper-ocean
528 stratification (Fedorov et al., 2015), which affects precipitation changes, including reduced rainfall
529 in northwest Australia (Brierley et al., 2009; Burls & Fedorov, 2017). The IPWP underwent a
530 steplike transition between 1800 and 1600 ka (Bali et al., 2020; Martínez-Garcia et al., 2010) from
531 an expanded tropical warm pool which persisted in the Pliocene to a reduced warm pool, due to
532 the expansion of the subpolar water masses (Martínez-Garcia et al., 2010). To investigate the
533 connection between the warm pool change and the transition observed at U1483, we evaluate
534 changes in SST gradients between the IPWP center and its edge (Figures 2 and S13). The SST
535 record from the warm pool (Site 806) shows a gradual increase in SSTs compared to those from
536 off-center sites (Sites 722, U1460, 1146 and 846), which exhibit subtle decreases/increases
537 between 1800 and 1500 ka (Figure S13). Our results suggest that the enhanced zonal SST gradient
538 (White & Ravelo, 2020) is coupled to enhanced gradients between the center of the warm pool and
539 peripheral sites from ~ 1800 to 1500 ka (Figure 2). This result indicates that the contraction of the
540 warm pool starting at ~ 1800 ka and culminating in the establishment of the modern warm pool

541 pattern at ~ 1500 ka, is closely coupled to the development of the modern cold tongue and Walker
542 circulation (Kaboth-Bahr & Mudelsee, 2022; Martinez-Garcia et al., 2010).
543   The observed warm pool contraction occurred at roughly the same time as the observed
544 aridification (Figure 2) of northwest Australia at 1700 - 1400 ka. Contraction of the warm pool
545 enhanced both the zonal and meridional temperature contrast and strengthened the atmospheric
546 meridional Hadley circulation causing stronger trade winds (Brierley et al., 2009). Model
547 simulations have shown that the strength of the meridional SST gradients, particularly between the
548 subtropics and the tropics, plays a key role in driving hydrological changes in the warm Pliocene
549 experiment through controlling the strength of the Hadley circulation (Brierley et al., 2009; Burls
550 & Fedorov, 2017). These simulations point out that the wetter subtropics in the Pliocene are the
551 result of weakened equatorward moisture transport due to the reduced meridional circulation
552 (Burls & Fedorov, 2017). Therefore, the intensification in the large-scale meridional SST gradient
553 and the warm pool contraction from 1800 to 1500 ka, could have induced an enhanced wind-driven
554 meridional moisture transport resulting in reduced precipitation in the subtropics such as the
555 aridification in northwest Australia observed in our records. While intensification of the Walker
556 circulation and enhanced trade winds between 1500 and 1800 ka could theoretically cause an
557 increase in the ITF transport, existing SST records (e.g., He et al., 2021; Petrick et al., 2019; Smith
558 et al., 2020) documenting a weakening of the ITF suggest that sea level change was a more
559 important control on the ITF during this time.
560   The balance of evidence suggests that the contraction of the warm pool and associated
561 changes in rainfall patterns combined with the restriction of the ITF due to sea level changes and
562 the Asian monsoon feedback reduced moisture supply to northwest Australia, leading to
563 aridification and reduced terrigenous flux at U1483 from ~ 1700 to ~ 1400 ka.

5.2 The 1700 - 1400 ka transition in productivity

565   The long-term evolution of productivity, monitored using TN MAR (Figure 2), indicates a
566 decrease in productivity from ~ 1700 to ~ 1400 ka. Within this interval, there is a marked shift at
567 ~ 1650 ka in the other productivity indicators, total C_{37} (Figure S6) and $RABD_{660}$ (Figure 3 and
568 Table 1), and a less distinct shift toward higher values in the indicators of bottom water oxygen
569 conditions, Log (Mn/S) and U (Figure 3 and Table 1). The $\delta^{13}C_{org}$, bulk $\delta^{15}N$ and TOC:TN ratios
570 suggest minimal terrigenous derived organic matter and inorganic N contribution at U1483 (see
571 section 4.1.4 and Figure S7); thus we interpret the TN MAR record as reflecting a primarily marine
572 source, consistent with palynological analysis from the nearby site MD01-2378 (Holbourn et al.,
573 2005). Generally, our productivity proxies show significant correlation with oxygen proxies from
574 2000 to 1300 ka (Tables 2 & 3), probably explained by the fact that dissolved oxygen consumption
575 is influenced by surface productivity with relatively low oxygen related to high productivity and
576 vice versa. Differences between these proxy records might be related to independent changes in
577 the deep circulation or preformed oxygen.
578   In the modern ocean, the upper ocean mixing and productivity in the Timor Sea are affected
579 by the ITF transport and monsoonal winds. Thus, to explain the 1700 - 1400 ka transition observed
580 in the productivity-related proxy records (Figures 2 & 3), we explore three processes. **1)** The
581 Australian winter offshore monsoon winds lead to intense Ekman transport and enhanced
582 upwelling and productivity along the coast in northwest Australia (Beaufort et al., 2010; Susanto
583 et al., 2001). The strong precession cycles in productivity changes driven by offshore monsoon
584 winds have been documented in the Timor Sea and Banda Sea over the late Pleistocene by
585 Holbourn et al. (2005) and Beaufort et al. (2010). **2)** An enhanced ITF would increase the upper

586   ocean stratification along the west Australian coast by bringing warm and fresh water from the
587   Pacific and suppress the coastal upwelling and productivity. During cold and dry glaciations, lower
588   sea levels resulted in a restricted and weakened ITF and led to an increase in upwelling and
589   productivity (Susanto et al., 2001). It has been shown that productivity in the Timor Strait is
590   strongly inversely proportional to the intensity of ITF over the last glacial cycle (Müller & Opdyke,
591   2000). **3)** The nutrient supply from Pacific source water can affect productivity. The upper waters
592   in the Timor Sea mainly originate from the North Pacific through the ITF and the intermediate
593   water comprises Indonesian intermediate water and the AAIW from the South Pacific (Chen et al.,
594   2022 and references therein). In sum, the transition to lower productivity from ~ 1700 to ~ 1400
595   ka at U1483 could be the result of **1)** a reduction of the strength of the Australian winter monsoon;
596   **2)** an increase in the intensity of the ITF; and/or **3)** the reduction of nutrient supply from the source
597   water.

5.2.1   Shift in Australian winter monsoon and in the ITF

599   The intensification in Walker and Hadley circulation (see section 5.1.3) and the reduction
600   in the ITF (see section 5.1.2) would be expected to be accompanied by an increase in productivity
601   from ~ 1700 to ~ 1400 ka, which is the opposite of what is observed in our productivity related
602   records (Figures 2 & 3). Enhanced Walker and Hadley circulation strengthen the trade winds, thus
603   there was likely a strengthening in the Australian winter monsoon (Wang et al., 2005) at the
604   transition. This is supported by observations of the intensification of coastal upwelling off the
605   northwest Australian coast since ~ 1700 ka (Smith et al., 2020), however this intensification of
606   upwelling is not coupled to an increase in productivity. The restriction of the ITF documented
607   during ~ 1700 - 1500 ka is expected to enhance the upwelling and the productivity through
608   reducing the stratification of the upper ocean in the Timor Sea. However, while the reduction of
609   the ITF could contribute to surface cooling and the decrease in the terrigenous input and
610   precipitation (see section 5.1.2), it cannot explain the reduction observed in our productivity
611   records (Figures 2 & 3; Table 1). Therefore, the shift to lower productivity during the transition
612   was not forced by physical processes such as those related to the winter monsoon and the effects
613   of the ITF on stratification; rather, the lower productivity has to be related to reduced nutrient
614   concentration of the source water.

5.2.2   Productivity changes related to source water process

616   The development of modern-like Walker circulation and IPWP at roughly 1700 - 1400 ka
617   was accompanied by transitions observed in many global oceanic and continental records (Berner
618   et al., 2022; Etourneau et al., 2009, 2013; Fang et al., 2020; Lawrence et al., 2006; Li et al., 2011;
619   Ravelo et al., 2004; Wang et al., 2010). Our U1483 productivity record shows striking similarities
620   to that from ODP Site 846 located in the east equatorial pacific (EEP) (Figure 2) (Lawrence et al.,
621   2006). At Site 846, the $U^{K'}_{37}$ - based SST record shows cooling at ~ 1650 ka (Figure S12) and the
622   total C_{37} productivity record exhibits a transition between 1700 - 1400 ka, which is similar to our
623   U1483 record and to records at site ODP 1012 in the California Margin (Liu et al., 2008) and other
624   EEP sites (Site 1239 and 1240) (Etourneau et al., 2013). Furthermore, the productivity records
625   from EEP site 846 and our northwest Australian site U1483 both show similar glacial-interglacial
626   patterns after ~ 1600 ka. These similarities among distant sites support the idea that the transition
627   in the productivity records is primarily driven by similar nutrient source water changes instead of
628   separate regional changes.
629   Lawrence et al. (2006) propose that the transition to lower productivity in the mid-
630   Pleistocene might be related to the development of the modern Southern Ocean opal belt at ~ 2000

631   ka (Cortese et al., 2004), consistent with the idea that the Southern Ocean may play an important
632   role in the 1600 ka Plio-Pleistocene transition (Wang et al., 2010). Etourneau et al. (2013)
633   attributed the termination of the high productivity interval at EEP sites to enhanced regional
634   denitrification and decreased nutrient leakage from the high latitude regions, associated with high
635   productivity in the Southern Ocean due to iron fertilization between ~ 1700 and 1600 ka (Martínez-
636   Garcia et al., 2011). As such, relatively low nutrient water was transported to the low latitude
637   regions via the mode and intermediate waters and limited production in the equatorial Pacific
638   (Lawrence et al., 2006; Martínez-Garcia et al., 2011). Since water at U1483 is mainly derived from
639   the Pacific, including North Pacific upper waters and AAIW, we concur with the previous
640   interpretations that the transition in the productivity records observed at U1483 could be attributed
641   to the decreased nutrient supply in the water sourced from high latitude regions, related to the
642   increased production in the Southern Ocean due to the enhanced iron fertilization (Martínez-Garcia
643   et al., 2011) and extensive diatom mat development at ~ 1900 ka (Cortese & Gersonde, 2008). We
644   note that the pronounced decrease TN MAR occurred while $CaCO_3$ MAR increased at 1600 - 1650
645   ka at U1483 (Figure S5), likely indicating an ecosystem shift during this period. We conclude that
646   the transition in productivity at U1483 from ~ 1700 to ~ 1400 ka reflects changes in Pacific source
647   waters, associated with Southern Ocean biogeochemical dynamics and the nutrient redistribution
648   of the global ocean.

5.3   Orbital variability

650   Orbital resolution records generated between ~ 2000 and ~ 1300 ka at U1483 reveal a shift
651   in orbital characteristics between ~ 1650 and 1625 ka. Due to the appearance of this striking shift
652   spectral analysis was performed on two time intervals (before and after ~ 1625 ka). This shift,
653   explained in more detail in the following sections is characterized by 1) a change in terrigenous
654   input and productivity orbital variability from weak cyclicity prior to 1625 ka to strong cyclicity
655   after 1625 ka (Figure 4); 2) a change from weak coherence between terrigenous input proxies and
656   precession prior to ~ 1650 ka to stronger coherence after ~ 1650 ka (Figure 5); 3) a change in
657   productivity and oxygen variability from being coherent to orbital forcing at the precession band
658   prior to ~ 1650 ka to being coherent with orbital forcing at the obliquity band after ~ 1650 ka
659   (Figure 5). In all, the orbital variability analysis reveals a significant transition period during which
660   the proxy records started to become more sensitive to orbital forcing between ~ 1650 and 1625 ka
661   (see section 5.3.5). In the sections below, we discuss the processes potentially responsible for the
662   orbital scale variability at U1483.

5.3.1   Terrigenous input obliquity-band variability

664   Obliquity variability in the U1483 terrigenous input records (inferred by K wt% and Log
665   ((Al+K+Ti+Fe)/Ca)) is weakly coherent with obliquity from 1625 to ~ 1300 ka (Figures 4 & 5),
666   similar to results over the last 410 kyr at the same site (Zhang et al., 2020). Gong et al. (2023)
667   pointed out that precipitation and terrigenous input variation at U1483 was dominated by
668   precessional signal from 1600 to ~ 950 ka by using the same proxy (Log ((Al+K+Ti+Fe)/Ca))).
669   This inconsistence comes from the evolution of the precipitation variability on orbital timescale:
670   from ~ 1600 to 1300 ka, K wt% and Log ((Al+K+Ti+Fe)/Ca)) exhibit both obliquity (stronger)
671   and precession cyclicities; from 1300 to ~ 950 ka, they exhibit pronounced precession cyclicity.
672   Therefore our results suggest that precipitation variations in northwest Australian are driven by
673   combined precession and obliquity forcing. The weak coherency between our records and
674   obliquity is likely related to a non-stationary phase relationship between terrigenous input and

675　obliquity forcing (Figure S14). In contrast to the nearly anti-phase relationship between the rainfall
676　record and obliquity forcing over the last 410 kyr at U1483 (Zhang et al., 2020), our terrigenous
677　input records are roughly aligned with obliquity variations from 1625 to ~ 1300 ka (Figure S14),
678　consistent with wetter interglacial periods (obliquity max) and drier glacial periods (obliquity min),
679　which is supported by continental climate variability in Australia during the Pleistocene that have
680　been attributed to high sea levels and potential enhanced monsoon activity (Kershaw et al., 2003a,
681　2003b; Martin, 2006 and references therein). There is little obliquity forcing in the local low-
682　latitude insolation (Figure 4), but obliquity is significant in NH high-latitude insolation driving
683　glacial-interglacial sea level variability in the 40 kyr world. In this context, the obliquity signal in
684　our terrigenous input records could be related to obliquity band variations in **1)** the Walker
685　circulation and the ITF regulated by sea level effects on the exposure of the Maritime continent;
686　**2)** the Walker circulation and the ITF driven by tropical Pacific dynamics; **3)** latitudinal migration
687　of the ITCZ.
688　　　The first two mechanisms causing the obliquity-paced variability in the northwest
689　Australian precipitation and terrigenous flux are related to changes in the Walker circulation and
690　the ITF; these two processes produce opposite effects. In the first mechanism, precipitation in the
691　warm pool region is driven by the Walker circulation regulated by the landmass configuration of
692　the Maritime Continent on glacial-interglacial timescales (DiNezio et al., 2016; DiNezio &
693　Tierney, 2013; Du et al., 2021). Based on the last glacial maximum (LGM) records and model
694　simulations, low sea level in the glacial times led to more land exposure of the northwest Australian
695　shelf and Sunda and Sahul shelves [shallow < 50 m] (Figure 1), inducing reduced convection due
696　to enhanced land cooling over exposed areas, thus leading to weakening of the ascending branch
697　of the Walker circulation over the Maritime continent and dry eastern Indian Ocean and northwest
698　Australian regions (DiNezio et al., 2016; DiNezio & Tierney, 2013; Du et al., 2021). At the same
699　time, reduced ITF transport during low glacial sea level would have reinforced the influence of the
700　Walker circulation by modifying the moisture and heat reaching northwest Australia. From 1625
701　to ~1300 ka, glacial sea levels ranged from - 50 to - 85 m (Berends et al., 2021 and references
702　therein), therefore substantial change in the land-sea configuration could have led to glacial-
703　interglacial variation in the Walker circulation, the ITF transport and northwest Australian
704　precipitation, which is generally reflected in our records. The second mechanism by which
705　precipitation is affected by the Walker circulation and the ITF is related to obliquity-driven
706　changes in the tilt or depth of the EEP thermocline through the Plio-Pleistocene (Lawrence et al.,
707　2006). In this hypothesis, high (low) obliquity is related to a deep (shallow) thermocline and warm
708　(cool) EEP SSTs, resulting in a weaker (stronger) Walker circulation and ITF and consequently in
709　reduced (enhanced) convection (rainfall) over Maritime Continent and north Australia (Feng et al.,
710　2018; Lawrence et al., 2006). This Pacific dynamical mechanism is opposite to our observations
711　and therefore is likely to be outpaced by the first (sea level-Maritime continent exposure)
712　mechanism; we conclude that obliquity-paced precipitation in the northwest Australian region was
713　primarily governed by the regional processes regulated by sea level changes.
714　　　The third mechanism that may explain variations in northwest Australian precipitation is
715　associated with the latitudinal migration of the ITCZ. Obliquity forcing may have played a critical
716　role in driving the south-north migration of the West Pacific ITCZ and modulating the precipitation
717　pattern in the tropical Pacific during the late Quaternary (Liu et al., 2015; Zhang et al., 2020). Site
718　U1483 is located at the southern margin of the modern Indo-Pacific ITCZ where rainfall is
719　sensitive to its latitudinal migration. The cross-hemispherical thermal pressure contrast between
720　the Siberian High and the Australian Low was likely primarily driven by obliquity forcing, with

721 high obliquity leading to strong cross-equatorial northerly winds that pushed the ITCZ south
722 during the late Pleistocene (Liu et al., 2015). This could have strengthened the Australian summer
723 monsoon through the across-equatorial 'pressure-push' process in the coupled East Asian–
724 Australian circulation system (An, 2000; Liu et al., 2015). The terrigenous records at Site U1483
725 are generally consistent with the notion that intensified rainfall occurred at high obliquity due to
726 the southward migration of the ITCZ and enhanced Australian summer monsoon.

727 In summary, the glacial-interglacial obliquity signal in precipitation in northwest Australia
728 from 1625 to ~ 1300 ka is likely associated with changes in the Walker circulation and the ITF
729 driven by sea level changes, possibly combined with the latitudinal migrations of the ITCZ. In this
730 study, we are not able to distinguish those two mechanisms. To further understand ITCZ 40 kyr
731 variations across the Indo-Pacific region will require reconstructions of spatial patterns using
732 multiple sites. It is not clear how to explain the evolution of the phase relationship between the
733 precipitation proxies and obliquity forcing (including the lead of precipitation over obliquity
734 maximum between 1600 – 1350 ka (Figure S14)); perhaps it results from the combination of
735 different mechanisms mentioned above and/or related to the inherent errors (4 - 6 ka) of the LR04
736 age model (Lisiecki & Raymo, 2005).

5.3.2 Terrigenous input precession-band variability

738 At U1483, terrigenous input records (inferred by K wt% and Log ((Al+K+Ti+Fe)/Ca))
739 exhibit precessional band (19-23 kyr) variance from ~ 2000 to ~ 1300 ka, which becomes stronger
740 and coherent with precessional forcing after 1625 ka (Figures 4 & 5). Between 1625 and 1300 ka,
741 terrigenous input proxies lag precession minimum by ~ 1 - 2 kyr (Figure 6) and are therefore almost
742 out of phase with local summer insolation (Jan-Feb_20S) and in phase with boreal summer
743 insolation (Jul-Aug_10N) (Figures 6 & S15), consistent with the precipitation precessional
744 variation over the last 1600 ka from the same site (Gong et al., 2023; Zhang et al., 2020). This high
745 coherence and phase relationship indicate that instead of being governed by local summer
746 insolation, precipitation in the northwest Australian region was strongly coupled to NH tropical
747 dynamics at precession band in the 40 kyr world. We investigate three plausible underlying
748 mechanisms causing the precession-paced variability in northwest Australian precipitation and
749 terrigenous flux: **1)** expansion and contraction of the ITCZ; **2)** Walker circulation variability; **3)**
750 Indian Ocean Dipole (IOD) dynamics.

751 The first mechanism that may explain the precessional signal in northwest Australian
752 precipitation is associated with the ITCZ dynamics. Although local insolation directly affects the
753 local land-ocean thermal contrasts and the intensity of the ITCZ, the fact that precessional
754 variability in U1483 precipitation proxy records is out of phase with local insolation indicates that
755 this process was not the primary factor in controlling the rainfall pattern in this region. Instead,
756 based on the above discussions, precipitation in northwest Australia is sensitive to the latitudinal
757 migration of the ITCZ which is sensitive to hemispheric contrasts in temperature and pressure. As
758 such, based on the in-phase precipitation pattern between the two hemispheres, Zhang et al. (2020)
759 point out that the precessional cyclicity in terrigenous discharge at U1483 was driven by the
760 contraction and expansion of the ITCZ regulated by precession forcing over the last 410 kyr,
761 supported by the modeling study of Singarayer et al. (2017). The modeling results suggest that the
762 marine ITCZ displays expansion and contraction with precessional cyclicity in response to the
763 interhemispheric temperature gradients during the late Quaternary (Singarayer et al., 2017).
764 During weak precession, when boreal summer is warmer and boreal winter is cooler, increased
765 interhemispheric temperature gradients cause the ITCZ to move further north during the boreal
766 summer and further south during the boreal winter, leading to the expansion of the rain belt and

767 vice versa. This is in agreement with our results, which show enhanced precipitation at the southern
768 margin of the ITCZ (U1483) during minimum precession. Due to the limit of ^{230}Th dating, there
769 is no cave stalagmite record with an independent age model in the mid-early Pleistocene, thus we
770 could not further test whether the idea of Zhang et al. (2020) applies to the 40 kyr world. Additional
771 precipitation records from the northern margin and heart of the ITCZ/warm pool during the 40 kyr
772 world will help to test this idea. In sum, based on available information, precessional variability in
773 our terrigenous input records from 1625 to ~ 1300 ka is potentially due to the expansion and
774 contraction of the ITCZ.

775   The second possible mechanism causing the observed precessional variance in
776 precipitation records at U1483 is related to insolation-forced changes in the Walker circulation.
777 We concur with the previous interpretation that precessionally driven changes in warm pool heat
778 storage and the Walker circulation was likely to regulate the terrigenous input variability from
779 1625 to ~ 1300 ka (Gong et al., 2023). At precession minima, summer (boreal) solstice occurs at
780 perihelion (maximum Jul-Aug insolation in the tropics), corresponding to warm NH summers and
781 warm SH winters, and the warm pool warms and expands, possibly leading to increased zonal
782 upper thermal contrast and enhanced Walker circulation (La Niña-like). Therefore, increased
783 precipitation should occur at precession minima in the west warm pool, including the northwest
784 Australian region. In fact, Jian et al. (2022) found that the upper ocean heat content of the IPWP
785 exhibited pronounced precession cycles and the maximum heat storage lagged precession minima
786 by ~ 3 kyr during the 100 kyr world and attributed their observations to stronger Walker circulation
787 occurring at precession minima driven due to increased upper ocean heat content of the IPWP (Jian
788 et al., 2022). This idea is further supported by observations of precession-minima-associated
789 deeper thermocline in the western equatorial Pacific in the late Quaternary (Lo et al., 2022). We
790 find that precipitation variability in the 100 kyr world at U1483 (Zhang et al., 2020) has the same
791 precessional variability and phase relative to insolation compared to our records from the 40 kyr
792 world (Figures 6 & S15); thus, precessional changes in the Walker circulation documented in the
793 100 kyr world (Jian et al., 2022; Lo et al., 2022) may also explain precession-paced variability in
794 precipitation during the 40 kyr world.

795   The third mechanism relevant to precipitation variability at U1483 is related to the Indian
796 Ocean Dipole (IOD) dynamics, which influence the hydroclimate in the eastern Indian Ocean and
797 the Timor Sea. A previous modeling study indicates that the frequency and amplitude of the
798 positive phase of the IOD is driven by the solar insolation of the north tropical region and is
799 proportional to the seasonality in the mid-Holocene (Iwakiri & Watanabe, 2019). In this context,
800 at precession minima, NH seasonality is strong, leading to strong positive IOD in boreal summer
801 and drought in the east Indian Ocean, which is the opposite of our precipitation records at U1483.
802 Thus, precessional variation in our records is not likely to be driven by changes in the IOD.
803 However, IOD evolution is poorly understood in the 40 kyr world due to the lack of records and
804 model simulations in the Indian Ocean. In summary, we conclude that the dominant precession
805 variance in precipitation at Site U1483 from 1625 to ~1300 ka is likely induced by the expansion
806 (contraction) of the ITCZ and/or the precession-regulated Walker circulation.

807   Moreover, although it is known that Australian summer monsoon is impacted by the Asian
808 monsoon system, we do not discuss the phase relationship between Asian winter monsoon and our
809 records in this study because the available orbitally-resolved Asian monsoon records are tuned to
810 the orbital template when building the age model (Sun et al., 2006). However, it is worth pointing
811 out that the available EAWM record does show similar orbital cyclicity and some coherence with
812 our terrigenous input proxy both on obliquity and precession bands from ~ 1600 to ~ 1300 ka

813 (Figures S10 & S16). We note that the striking shift in terrigenous input occurred at ~ 1640 ka at
814 U1483 during the transition from glacial_58 (MIS 58) to interglacial_57 (MIS 57); this
815 corresponds to the shift from one major glacial loess horizon (L24) to an interglacial paleosol
816 horizon (S23), associated with reduced Asian winter monsoon during deglaciation on orbital
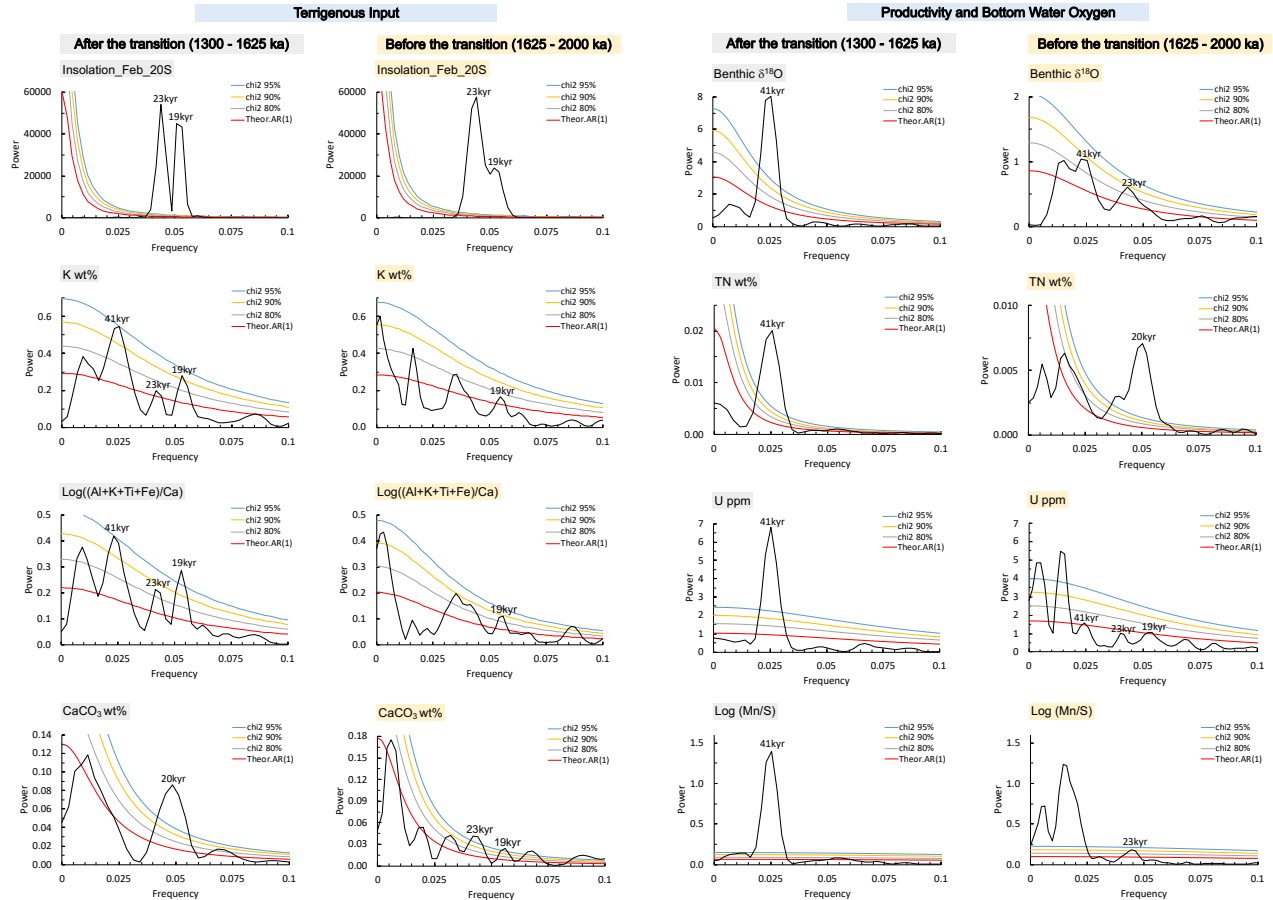817 timescale (Ding et al., 2002; Sun et al., 2006, 2019).

5.3.3 Productivity obliquity-band variability

819 At U1483, productivity (TN wt%) and bottom water oxygen (U and Log (Mn/S)) proxies
820 show pronounced power concentrated at the obliquity band from 1625 to ~ 1300 ka (Figure 4); the
821 records are strongly coherent with obliquity forcing and benthic $\delta^{18}O$, with productivity minima
822 lagging $\delta^{18}O_{min}$ by ~ 1.6 - 2.7 kyr (Figures 5 & 6). From 1625 to ~ 1300 ka, high productivity and
823 low bottom water oxygen characterized glacial periods and vice versa (Figures 3 & S14). We
824 attribute the glacial-interglacial variations in local productivity to changes in upwelling strength,
825 which could be driven by the intensity of the ITF regulated by sea level changes and/or the strength
826 of the Australian offshore winter monsoon. During glacial times, lower sea level and weak Walker
827 circulation resulted in reduced ITF transport (DiNezio et al., 2011, 2016), leading to reduced
828 stratification of the upper ocean in the Timor Sea and thus increased upwelling and productivity.
829 The alternative mechanism is associated with the Australian winter monsoon, the offshore wind
830 enhanced by the easterly trade winds. Productivity variability lags obliquity forcing and is nearly
831 in phase with $\delta^{18}O$, suggesting that it is likely ultimately tied to global glacial-interglacial changes,
832 rather than regional processes alone. During glacial times, changes in the large-scale atmospheric
833 circulation caused strong Australian winter monsoon, which could induce enhanced coastal
834 upwelling in the northwest Australian region and therefore high glacial productivity (Gong et al.,
835 2023). We cannot distinguish between those two mechanisms (ITF versus wind-induced
836 upwelling) in this study: both are tightly linked to glacial/interglacial changes as reflected in the
837 benthic $\delta^{18}O$ signal and could reinforce each other. In sum, at U1483, obliquity-paced variability
838 in productivity is strongly coherent and nearly in-phase relationship with the $\delta^{18}O$ signal
839 suggesting that productivity variability in the Timor Sea was driven by the changes in intensity of
840 the ITF related to sea level changes and/or in the strength of the offshore winds from 1625 to ~
841 1300 ka.

5.3.4 Productivity precession-band variability

843 Productivity (TN wt%) and bottom water oxygenation (U and Log (Mn/S)) proxies at
844 U1483 only show precessional variance from 2000 to 1625 ka, similar to the behavior of benthic
845 $\delta^{18}O$ (Figure 4). Specifically, from ~ 1900 to 1700 ka, benthic $\delta^{18}O$, productivity and oxygenation
846 proxies exhibit strong coherence with precession (Figure 5), with productivity (TN wt%) lagging
847 benthic $\delta^{18}O$ by 1.8 (± 1.8) kyr. This coupling between productivity/oxygenation proxies and
848 benthic $\delta^{18}O$ is similar to what was found in the obliquity band, suggesting that the precession
849 signal in productivity was likely controlled by the intensity of the ITF regulated by sea level
850 changes and/or the strength of the Australian offshore winter monsoon (see section 5.3.3). Because
851 of the low resolution of available sea level reconstructions during this time interval, it is not
852 possible to resolve precessional variations in sea level change though there seems to be orbital
853 band variations between 2000 to 1700 ka (Rohling et al., 2014). For this reason, we rely on the
854 benthic $\delta^{18}O$ record as an adequate reflection of global climate and sea level variability, and thus
855 our results showing a shift in productivity at U1483, from a dominant precession periodicity to a

856 dominant obliquity periodicity at ~ 1625 ka, was strongly linked to a shift in periodicity in global
857 ice volume changes and its influence on the strength of the ITF.
858

859
860
861 **Figure 4.** Spectral analysis results of different proxies before (highlighted by yellow) and after (highlighted by grey)
862 ~ 1625 ka. Except for insolation (Feb_20S), all other proxies are reconstructed from Site U1483. Spectral analysis
863 was performed using REDFIT with Blackman-Harris window (Oversample=2; Segments=2) from software program
864 Past 4 (Hammer, et al., 2001). Spectral analysis results of other proxies are shown in supplementary Figure S10.

5.3.5   Change in climate sensitivity during the mid-early Pleistocene

866   Based on the discussions above, the orbital variability in terrigenous input and productivity
867 at U1483 reveals a significant transition period such that more power was concentrated at orbital
868 bands and was more coherent with orbital forcing after ~ 1650 ka (Figures 4 & 5). At the obliquity
869 band, the pronounced increase in sensitivity and coherence from ~ 1800 to ~ 1600 ka in our
870 productivity and bottom oxygen records has been observed in globally widespread records
871 (deMenocal, 1995; Lawrence et al., 2006; Li et al., 2011; Martinez-Garcia et al., 2010; Peterson et
872 al., 2020). To explain the increase in sensitivity to obliquity forcing, previous studies proposed
873 that orbital-scale pCO_2 change likely played a major role to coordinate the response of tropical
874 climate to high-latitude forcing, potentially through coupling with the enhanced iron fertilization-
875 CO_2 feedback due to increased subantarctic iron deposition (Herbert et al., 2010; Lawrence et al.,
876 2006; Martínez-Garcia et al., 2011; Peterson et al., 2020). Atmospheric pCO_2 feedbacks likely
877 amplify the climatic response to obliquity forcing as global ice expanded, resulting in a higher
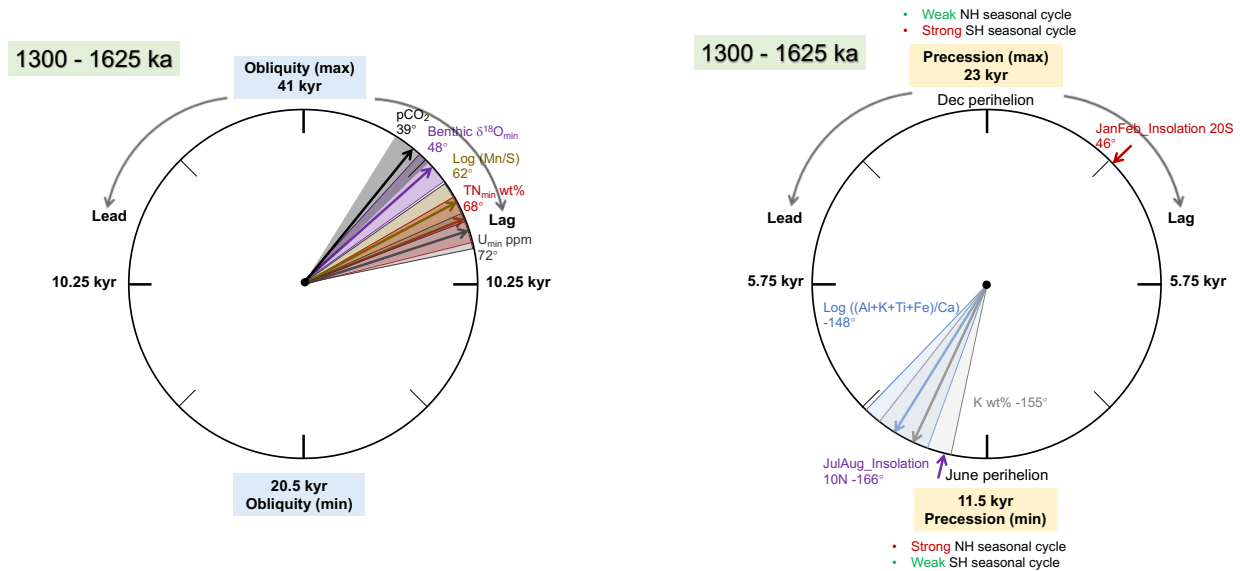878 sensitivity of the climate system to obliquity forcing. The recent published modeling-reconstructed

879 pCO_2 record shows strong obliquity band variance and coherence starting at ~ 1600 ka (Berends
880 et al., 2021) (Figure 5), supporting the proposed global greenhouse gas forcing mechanism.

881 At the precession band, different from the behavior of benthic $\delta^{18}O$ and modeling-
882 reconstructed pCO_2 (Berends et al., 2021) (Figure 5), our terrigenous input proxies show
883 pronounced coherence to precession after ~ 1650 ka. We attribute this to local feedbacks (e.g.,
884 Walker circulation) that amplified precession variance in the precipitation records. It is known that
885 a major reorganization occurred in the tropical oceans between 1800 and 1600 ka with
886 development of strong Walker circulation accompanied by shoaling of the thermocline (Ravelo et
887 al., 2004). The change of the mean state may have resulted in changes in local feedbacks that
888 amplified small perturbations in the solar forcing. For example, with average shoaled thermocline,
889 solar forcing could more readily affect the Walker circulation, resulting in precession band
890 variance in precipitation records.

891 Taken together, the striking appearance of 41 kyr obliquity cycles at ~ 1650 ka in our
892 productivity and oxygen records supports the notion that pCO_2 likely played a major role in driving
893 obliquity-band climatic variations in the mid-early Pleistocene. The increased coherence to
894 precession in our terrigenous input proxies after ~ 1650 ka is likely a result of local feedbacks.

Figure 5. Wavelet coherence analysis between proxies at U1483 (except the pCO$_2$ records from Berends et al. (2021)) and orbital forcing (obliquity and precession) from 1300 to 2000 ka. Wavelet coherence analysis was performed using biwavelet (wtc) package in R. The white dash lines indicate 19 kyr, 23 kyr and 41 kyr.

899

900
901 **Figure 6.** Phase wheel results of cross-spectral coherence and phase relationships at the obliquity band (left) and
902 precession band (right) from 1300 to 1625 ka. Clockwise phases indicate lags and counterclockwise phases indicate
903 leads. Shaded areas delineate error margins for U1483 records, modeled atmospheric pCO$_2$ from Berends et al., (2021).
904 We acknowledge that there are established phase lags built in the LR04 age model and the tuned benthic δ^{18}O record
905 displays almost the same spectral characteristics as the LR04 stack. In this study, we assume the built phase lags in
906 the age model are good assumptions and the relative phase relationship between proxies from the same site is robust.

907 ### 5.4 Nitrogen isotope variability

908   Based on the results of $\delta^{13}C_{org}$ and TOC:TN ratios (see section 4.1.4), the organic matter at
909 U1483 is primarily of marine origin with little terrestrial and inorganic N influences, and thus we
910 attribute variability in bulk δ^{15}N values to be primarily driven by marine processes. Site U1483 is
911 located in a relatively oligotrophic region, where surface nitrate is completely consumed on an
912 annual basis. The source of surface nitrate is mainly from the thermocline water that flows into the
913 Timor Sea as part of the ITF, upwells due to monsoonal winds (Alongi et al., 2011), and is
914 completely utilized. Therefore, δ^{15}N of organic matter in the sediment (bulk δ^{15}N) at U1483 should
915 be primarily controlled by the thermocline source water process (upwelled nitrate) instead of the
916 local primary production. However, a previous study found that lower bulk δ^{15}N occurred when
917 local productivity was high during the LGM and proposed that bulk δ^{15}N in the Timor
918 Throughflow could reflect glacial-interglacial changes in nitrogen utilization and potentially N$_2$
919 fixation (Müller & Opdyke, 2000). Thus, we investigate the influences of both changes in source
920 water and changes in local productivity on bulk δ^{15}N at U1483 over the last 2000 ka.

921   On long timescales, bulk δ^{15}N at U1483 exhibits no pronounced secular trend over the last
922 2000 ka and no significant transition between 1700 and 1400 ka, when productivity started to shift
923 to lower values (Figure 2, Table1); therefore, trends in bulk δ^{15}N are decoupled from trends in
924 productivity. This is different from observations at EEP Sites 1239 and 1240, which show that the
925 productivity shift at ~ 1600 ka is coupled to a shift in bulk δ^{15}N (Etourneau et al., 2013), suggesting
926 local nitrate utilization is an important factor in driving bulk δ^{15}N in the EEP but not at U1483.
927 Instead, the secular long-term trend in bulk δ^{15}N at U1483 reflects changes in the source
928 thermocline water. This is supported by the fact that U1483 exhibits similar trends to the bulk δ^{15}N
929 records from distant Site 1012 (located in the California margin) over the last ~ 2000 kyr (Figure
930 2) and from Site U1486 (located in the Bismarck Sea north of New Guinea) over the last ~ 1400

931 ka (Lambert et al., 2022). Since the upper thermocline waters in the Timor Sea are mostly sourced
932 from the North Pacific (Talley & Sprintall, 2005), this result indicates that bulk δ^{15}N at U1483 is
933 controlled by the changes in source water over long timescales during the Pleistocene epoch. Bulk
934 δ^{15}N records from Sites 1012 and U1486 are reported to primarily reflect denitrification change in
935 the Eastern Tropical Pacific (ETP) oxygen minimum zones (OMZs) during the Pleistocene, as a
936 result of remineralization of organic matter exported from ETP OMZs leading to zonally spreading
937 denitrification signals across the Pacific (Lambert et al., 2022; Liu et al., 2005). Based on the
938 striking similarity in long δ^{15}N bulk records between Sites U1483 and 1012, we concur with the
939 interpretation that denitrification signals from ETP are transported westward across the Pacific (Jia
940 & Li, 2011; Lambert et al., 2022), driving the bulk δ^{15}N variation in the Timor Sea. Notably, there
941 is a general offset of ~ 1‰ - 3‰ in δ^{15}N values between Sites U1483 (average = 6.5‰), 1012
942 (average = 7.7‰) and U1486 (average = 9.6‰) over the last ~ 1400 kyr; lower bulk δ^{15}N values
943 at U1483 potentially reflect the prevalence of local N_2 fixation in the Timor Sea (Müller & Opdyke,
944 2000).
945   Orbital variations in the bulk δ^{15}N record at U1483 generally exhibit different spectral
946 power features and correlations with TN wt% from 2000 to 1300 ka (Figure S10), although there
947 are some intervals that indicate coherent variability and therefore potentially some local controls
948 of productivity on bulk δ^{15}N. Between 2000 and 1625 ka, bulk δ^{15}N shows significant negative
949 correlation with productivity (oxygen) proxies (Figure S17, Table 2 & 3) and high coherence with
950 the productivity index (TN wt%) at the 19-23 kyr (precession) band from ~1650 to 1750 ka and at
951 ~1850 ka (Figure S18). During those specific time intervals, lower δ^{15}N occurs during higher
952 productivity periods, indicating changes in local N utilization likely leading to the precessional
953 variations in bulk δ^{15}N records, probably related to precession-driven sea level changes. After ~
954 1750 ka, bulk δ^{15}N at U1483 shows high coherence with bulk δ^{15}N at Site 1012 both at the 41 kyr
955 (obliquity) and 19-23 kyr (precession) bands and little coherence (and correlation) with
956 productivity index (TN wt%) (Figures S17 & S18, Tables 2 & 3), suggesting that bulk δ^{15}N
957 variation at U1483 is dominated by source water processes during this period. Liu et al. (2005)
958 attributed the obliquity variation in bulk δ^{15}N and SST at Site 1012 to high latitude forcing
959 modulation of thermocline conditions, including the strength of denitrification, throughout the
960 Plio-Pleistocene. Diz & Pérez-Arlucea, (2021) proposed that 41 kyr glacial-interglacial variability
961 in bulk δ^{15}N record records from OMZs during the middle Pleistocene is caused by enhanced
962 glacial ventilation of tropical thermocline due to increased AAIW influence. In terms of the
963 precessional variability, previous proxy and modeling studies indicated that precession has a strong
964 impact on tropical Pacific thermocline depth and upwelling strength (Clement et al., 1999; Rafter
965 & Charles, 2012), which could lead to the 19-23 kyr signals observed in denitrification records
966 (Kong et al., 2021; Lacerra et al., 2021). We note that the bulk δ^{15}N record at U1483 does not
967 exhibit the relatively high peak values that appear in the 1012 record (e.g., ~ 1430 ka, ~ 1560 ka)
968 (Figure 2). The differences in amplitudes and peak values between those two records could be
969 related to the modification of source water while transferring from the Pacific to the Timor Sea
970 and/or associated with offsetting local denitrification isotopic effects.
971   In summary, our results reveal striking similarities in bulk δ^{15}N records between Sites
972 U1483 and 1012, suggesting that bulk δ^{15}N in the Timor Sea was primarily driven by changes in
973 the source water from the North Pacific at orbital and longer timescales, reflecting denitrification
974 changes in the ETP. In some specific intervals, orbital variations in bulk δ^{15}N at U1483 also likely
975 reflect changes in local N utilization.

976   **5.5   Benthic carbon isotope interpretation**

977   In some cases, changes in surface productivity can be monitored by changes in deep ocean
978 chemistry such as benthic $\delta^{13}C$, which would be expected to decrease during times of stronger
979 organic matter export from the surface water and remineralization at depth. However, benthic $\delta^{13}C$
980 is also influenced by whole ocean changes in seawater $\delta^{13}C$ values and by deep water mass mixing.
981 At U1483, benthic $\delta^{13}C$ shows significant variance in the obliquity band (41 kyr) from 1625 to
982 1300 ka, and weak precessional variance (19-23 kyr) from 2000 to 1625 ka (Figure S10). Benthic
983 $\delta^{13}C$ exhibits similar behaviors to benthic $\delta^{18}O$ and it is strongly coherent with benthic $\delta^{18}O$ both
984 at the obliquity and precession bands from 2000 to 1300 ka (Figure 5). Benthic $\delta^{13}C$ also shows
985 strong correlation with U concentration at the obliquity band from 2000 to 1300 ka (Figure S9).
986 To understand if these observations are related to global rather than local effects, the benthic $\delta^{13}C$
987 record from U1483 is compared to that from ODP Site 849, which is a deep site (> 3800 m) located
988 in the east equatorial Pacific, representing mean Pacific Ocean $\delta^{13}C$ values (Lyle et al., 2019
989 (updated age model); Mix et al., 1995). These two records show striking similarities in absolute
990 values and orbital variations (Figure S9). Bottom water at U1483 ($\sim$ 1700 m) is likely derived from
991 the AAIW from the South Pacific and potentially influenced by the Indian Deep Water (Tomczak
992 & Godfrey, 2003). The consistency between the benthic $\delta^{13}C$ records from the two sites suggests
993 that benthic $\delta^{13}C$ at U1483 primarily reflects whole ocean changes as represented by deep Pacific
994 Site 849 at orbital and longer timescales in the mid-early Pleistocene. This is also reflected in the
995 pronounced decoupling between productivity (TN MAR) and bottom oxygen proxies (U and Log
996 (Mn/S)) from 1700 to 1650 ka (Figure S9), when bottom water oxygenation and benthic $\delta^{13}C$ are
997 governed by source water signals instead of local productivity. However, specifically during
998 interglacials before $\sim$ 1600 ka, benthic $\delta^{13}C$ at U1483 shows relatively higher values than that at
999 Site 849 (Figure S9). This interglacial offset indicates local processes may play a role in modifying
1000 the benthic $\delta^{13}C$ at U1483 before $\sim$ 1600 ka, potentially related to changes in deep water circulation
1001 leading to better ventilation in the Timor Sea.

1002 **6 Conclusions**

1003   We provide multiproxy reconstructions from Site U1483 to investigate hydroclimate and
1004 productivity changes in the Timor Sea (off northwest Australia) during the 40 kyr world of the
1005 mid-early Pleistocene. On the long-term, the decrease in terrigenous input from $\sim$ 1700 to $\sim$ 1400
1006 ka indicates increased aridification in the northwest Australian region. We argue that the restriction
1007 of the ITF due to lower glacial sea level and Asian monsoon feedbacks, combined with the
1008 contraction of the IPWP, reduced moisture supply and precipitation to northwest Australia, leading
1009 to aridification and reduced terrigenous flux from $\sim$ 1700 to $\sim$ 1400 ka. Productivity in the Timor
1010 Sea shifted to lower values during the transition from $\sim$ 1700 to $\sim$ 1400 ka, showing similarities to
1011 the trend at EEP Site 846. We conclude that the decline in productivity at U1483 reflects a decrease
1012 in nutrient supply from Pacific source waters, associated with nutrient redistribution in the global
1013 ocean at this time. On orbital timescales, our records reveal a significant transition in the sensitivity
1014 of the U1483 proxy records to orbital forcing after $\sim$ 1650 ka; orbital-scale pCO$_2$ changes and local
1015 feedbacks are likely to play important roles in driving obliquity- and precession-paced climatic
1016 variations. Terrigenous input proxy records (reflecting precipitation) at U1483 only show weak
1017 coherency with obliquity forcing from 1625 to $\sim$ 1300 ka. We conclude that the glacial-interglacial
1018 obliquity-paced precipitation in northwest Australia is likely associated with changes in the Walker
1019 circulation and the ITF regulated by sea level exposure of the Maritime continent, possibly
1020 combined with the latitudinal migrations of the ITCZ. At the precession band, terrigenous input

1021 records are strongly coherent with precession and are almost out of phase with local summer
1022 insolation from ~ 1650 to ~ 1300 ka. We attribute the precession-paced variability in precipitation
1023 to the expansion and contraction of the ITCZ and/or the precession-regulated changes in the
1024 Walker circulation. Orbitally-modulated variations in productivity (oxygen) in the Timor Sea are
1025 coherent with and nearly in-phase with the benthic $\delta^{18}O$ signal from 2000 to 1300 ka, with a shift
1026 from dominant precessional periodicity to dominant obliquity periodicity at ~ 1650 ka. Our results
1027 reveal that productivity variability in the Timor Sea was strongly linked to global ice volume
1028 changes, driven by changes in ITF intensity related to sea level changes and/or in the strength of
1029 offshore winds. The striking similarities in bulk $\delta^{15}N$ records between Sites U1483 and 1012
1030 indicate that changes in Pacific source water are the primary control on biogeochemical changes
1031 in the Timor Sea at orbital and longer timescales in the mid-early Pleistocene. This study offers
1032 new insights on hydroclimate and productivity evolution in northwest Australia and extends the
1033 history of ITF variability and Australian monsoon dynamics into the 40 kyr world of the mid-early
1034 Pleistocene.

1035

T-test before and after the transition (1300 - 2000 ka)							
1300 - 1625 ka	1625 - 2000 ka	Average		N (# observations)		P (two-tail)	Average from old to young
LR04 $\delta^{18}O$		3.82	3.76	151	150	0.0500	increase
Benthic $\delta^{18}O$		3.00	3.02	338	180	0.5700	decrease
TN wt%		0.09	0.12	101	150	<.0001	decrease
TN MAR		0.010	0.013	101	150	<.0001	decrease
U ppm		1.99	2.10	377	557	0.0006	decrease
Log (Mn/S)		-0.43	-0.55	1765	2087	<.0001	increase
$RABD_{660}$		0.06	0.07	1323	1566	<.0001	decrease
K wt%		0.94	1.13	377	557	<.0001	decrease
K MAR		0.10	0.13	377	557	<.0001	decrease
$CaCO_3$ wt% $_{EA}$		0.64	0.55	101	150	<.0001	increase
MAR $CaCO_3$		6.70	5.83	101	150	<.0001	increase
Log ((Al+K+Ti+Fe)/Ca)		-1.01	-0.82	1764	2087	<.0001	decrease
Bulk $\delta^{15}N$		6.00	6.15	101	150	0.0240	decrease
Benthic $\delta^{13}C$		0.004	0.025	330	154	0.3333	decrease

1036
1037 **Table 1.** A T-test table was created to analyze the significance of a change between averages for each proxy before
1038 and after the transition at 1625 ka from ~ 2000 to ~ 1300 ka. Except benthic $\delta^{18}O$, $\delta^{13}C$, U and bulk $\delta^{15}N$, all other
1039 proxies have significant changes (p < 0.0001) in their averages. All other productivity proxies (TN wt%, TN MAR,
1040 Log (Mn/S), $RABD_{660}$) and terrigenous input proxies (K wt%, K MAR, Log ((Al+K+Ti+Fe)/Ca), $CaCO_3$ wt% $_{EA}$)
1041 indicate lower productivity and lower terrigenous input after the transition.

1042

Correlation matrix before the transition 1300 - 1625 ka (R^2)	$CaCO_3$ wt% $_{EA}$	TN wt%	Bulk $\delta^{15}N$ (‰)	corresponding K wt%	corresponding U ppm	corresponding Log (Mn/S)	corresponding Log((Al+K+Ti+Fe)/Ca)	corresponding $RABD_{660}$
$CaCO_3$ wt% $_{EA}$	1.00							
TN wt%	0.06	1.00						
Bulk $\delta^{15}N$ (‰)	0.17	0.00	1.00					
corresponding K wt%	0.53	0.16	0.04	1.00				
corresponding U ppm	0.02	0.36	0.03	0.21	1.00			
corresponding Log (Mn/S)	0.02	0.53	0.00	0.08	0.28	1.00		
corresponding Log ((Al+K+Ti+Fe)/Ca)	0.86	0.11	0.16	0.66	0.05	0.05	1.00	
corresponding $RABD_{660}$	0.09	0.27	0.01	0.18	0.15	0.28	0.17	1.00

1043

Correlation matrix after the transition 1625 - 2000 ka (R^2)	$CaCO_3$ wt% $_{EA}$	TN wt%	Bulk $\delta^{15}N$ (‰)	corresponding K wt%	corresponding U ppm	corresponding Log (Mn/S)	corresponding Log((Al+K+Ti+Fe)/Ca)	corresponding RABD$_{660}$
$CaCO_3$ wt% $_{EA}$	1.00							
TN wt%	**0.24**	1.00						
Bulk $\delta^{15}N$ (‰)	0.10	**0.47**	1.00					
corresponding K wt%	**0.57**	0.13	0.05	1.00				
corresponding U ppm	0.07	**0.26**	0.12	0.17	1.00			
corresponding Log (Mn/S)	0.09	**0.40**	**0.23**	0.07	**0.28**	1.00		
corresponding Log ((Al+K+Ti+Fe)/Ca)	**0.83**	0.16	0.07	**0.69**	0.07	0.05	1.00	
corresponding RABD$_{660}$	**0.29**	**0.26**	0.08	**0.27**	**0.22**	**0.20**	**0.27**	1.00

1044
1045 **Table 2 & 3.** Correlation matrix tables were created in Excel by running a regression between pairs of proxies before
1046 (upper table) and after (bottom table) 1625 ka (using corresponding values due to proxies with different resolution).
1047 The R^2 values are listed and negatively correlated is denoted by purple, positively correlated is denoted by black;
1048 significantly correlated ($p < 0.0001$) is highlighted in yellow, not significantly correlated is highlighted in blue. The
1049 values we care about are denoted by bold.

1050 **Acknowledgments**

1057
1058
1059 **Data Availability Statement**
1060 Data associated with this study are archived at NOAA (working on the data archival process) and
1061 in Tables S1-S2.

1062
1063
1064 **References**

1065 Alongi, D. M., Edyvane, K., do Ceu Guterres, M. O., Pranowo, W. S., Wirasantosa, S., & Wasson, R. (2011).

1066   *Biophysical Profile of the Arafura and Timor Seas.* Report prepared for the Arafura Timor Seas Ecosystem

1067   Action (ATSEA) Program. 32ps.

1068 An, Z. (2000). The history and variability of the East Asian paleomonsoon climate. *Quaternary Science Reviews*,

1069   *19*(1–5), 171–187. https://doi.org/10.1016/S0277-3791(99)00060-8

1070 Auer, G., De Vleeschouwer, D., Smith, R. A., Bogus, K., Groeneveld, J., Grunert, P., Castañeda, I. S., Petrick, B.,

1071   Christensen, B., Fulthorpe, C., Gallagher, S. J., & Henderiks, J. (2019). Timing and Pacing of Indonesian

1072   Throughflow Restriction and Its Connection to Late Pliocene Climate Shifts. *Paleoceanography and*

1073   *Paleoclimatology*, *34*(4), 635–657. https://doi.org/10.1029/2018PA003512

1074   Bali, H., Gupta, A. K., Mohan, K., Thirumalai, K., Tiwari, S. K., & Panigrahi, M. K. (2020). Evolution of the

1075   Oligotrophic West Pacific Warm Pool During the Pliocene-Pleistocene Boundary. *Paleoceanography and*

1076   *Paleoclimatology*, *35*(11). https://doi.org/10.1029/2020PA003875

1077   Beaufort, L., van der Kaars, S., Bassinot, F. C., & Moron, V. (2010). Past dynamics of the Australian monsoon:

1078   Precession, phase and links to the global monsoon concept. *Climate of the Past*, *6*(5), 695–706.

1079   https://doi.org/10.5194/cp-6-695-2010

1080   Berends, C. J., de Boer, B., & van de Wal, R. S. W. (2021). Reconstructing the evolution of ice sheets, sea level, and

1081   atmospheric CO_2 during the past 3.6 million years. *Climate of the Past*, *17*(1),

1082   361–377. https://doi.org/10.5194/cp-17-361-2021

1083   Berner, N., Trauth, M. H., & Holschneider, M. (2022). Bayesian inference about Plio-Pleistocene climate transitions

1084   in Africa. *Quaternary Science Reviews*, *277*, 107287. https://doi.org/10.1016/j.quascirev.2021.107287

1085   Boyer, T. P., Garcia, Hernan E., Locarnini, Ricardo A., Zweng, Melissa M., Alexey ,V., Reagan, James R.,

1086   Weathers, Katharine A., Baranova, Olga K., Seidov, Dan, & Smolyar, Igor V. (2018). *World Ocean Atlas*

1087   *2018* (Temperature and Salinity). https://www.ncei.noaa.gov/archive/accession/NCEI-WOA18.

1088   Brierley, C. M., Fedorov, A. V., Liu, Z., Herbert, T. D., Lawrence, K. T., & LaRiviere, J. P. (2009). Greatly

1089   Expanded Tropical Warm Pool and Weakened Hadley Circulation in the Early Pliocene. *Science*,

1090   *323*(5922), 1714–1718. https://doi.org/10.1126/science.1167625

1091   Burls, N. J., & Fedorov, A. V. (2017). Wetter subtropics in a warmer world: Contrasting past and future

1092   hydrological cycles. *Proceedings of the National Academy of Sciences*, *114*(49), 12888–12893.

1093   https://doi.org/10.1073/pnas.1703421114

1094   Chang, C.-P., Wang, Z., & Hendon, H. (2006). The Asian winter monsoon. In *The Asian Monsoon* (pp. 89–127).

1095   Springer Berlin Heidelberg. https://doi.org/10.1007/3-540-37722-0_3

1096   Chen, X. Y., & Barton, C. E. (1991). Onset of aridity and dune-building in central Australia: Sedimentological and

1097   magnetostratigraphic evidence from Lake Amadeus. *Palaeogeography, Palaeoclimatology, Palaeoecology*,

1098   *84*(1–4), 55–73. https://doi.org/10.1016/0031-0182(91)90035-P

1099 Chen, Y., Xu, J., Liu, J., Li, T., Xiong, Z., Zhang, P., & Yan, H. (2022). Climatic and tectonic constraints on the

1100   Plio–Pleistocene evolution of the Indonesian Throughflow intermediate water recorded by benthic $\delta^{18}O$

1101   from IODP site U1482. *Quaternary Science Reviews*, *295*, 107666.

1102   https://doi.org/10.1016/j.quascirev.2022.107666

1103 Christensen, B. A., Renema, W., Henderiks, J., De Vleeschouwer, D., Groeneveld, J., Castañeda, I. S., Reuning, L.,

1104   Bogus, K., Auer, G., Ishiwa, T., McHugh, C. M., Gallagher, S. J., Fulthorpe, C. S., & IODP Expedition 356

1105   Scientists. (2017). Indonesian Throughflow drove Australian climate from humid Pliocene to arid

1106   Pleistocene. *Geophysical Research Letters*, *44*(13), 6914–6925. https://doi.org/10.1002/2017GL072977

1107 Clement, A. C., Seager, R., & Cane, M. A. (1999). Orbital controls on the El Niño/Southern Oscillation and the

1108   tropical climate. *Paleoceanography*, *14*(4), 441–456. https://doi.org/10.1029/1999PA900013

1109 Connock, G. T., Owens, J. D., & Liu, X.-L. (2022). Biotic induction and microbial ecological dynamics of Oceanic

1110   Anoxic Event 2. Communications Earth & Environment, 3(1), 136. https://doi.org/10.1038/s43247-022-

1111   00466-x

1112 Cortese, G., & Gersonde, R. (2008). Plio/Pleistocene changes in the main biogenic silica carrier in the Southern

1113   Ocean, Atlantic Sector. *Marine Geology*, *252*(3–4), 100–110. https://doi.org/10.1016/j.margeo.2008.03.015

1114 Cortese, G., Gersonde, R., Hillenbrand, C.-D., & Kuhn, G. (2004). Opal sedimentation shifts in the World Ocean

1115   over the last 15 Myr. *Earth and Planetary Science Letters*, *224*(3–4), 509–527.

1116   https://doi.org/10.1016/j.epsl.2004.05.035

1117 Dang, H., Wu, J., Xiong, Z., Qiao, P., Li, T., & Jian, Z. (2020). Orbital and sea-level changes regulate the iron-

1118   associated sediment supplies from Papua New Guinea to the equatorial Pacific. *Quaternary Science*

1119   *Reviews*, *239*, 106361. https://doi.org/10.1016/j.quascirev.2020.106361

1120 De Deckker, P., Barrows, T. T., & Rogers, J. (2014). Land–sea correlations in the Australian region: Post-glacial

1121   onset of the monsoon in northwestern Western Australia. *Quaternary Science Reviews*, *105*, 181–194.

1122   https://doi.org/10.1016/j.quascirev.2014.09.030

1123 deMenocal, P. B. (1995). Plio-Pleistocene African Climate. *Science*, *270*(5233), 53–59.

1124   https://doi.org/10.1126/science.270.5233.53

1125   De Vleeschouwer, D. (2017). *Natural Gamma Radiation-derived K, U and Th contents of marine sediments*

1126   *obtained during IODP Expeditions with DV JOIDES Resolution* [Data set]. Interdisciplinary Earth Data

1127   Alliance (IEDA). https://doi.org/10.1594/IEDA/100668

1128   DiNezio, P. N., Clement, A., Vecchi, G. A., Soden, B., Broccoli, A. J., Otto-Bliesner, B. L., & Braconnot, P. (2011).

1129   The response of the Walker circulation to Last Glacial Maximum forcing: Implications for detection in

1130   proxies: LGM WALKER CIRCULATION. *Paleoceanography*, *26*(3), n/a-n/a.

1131   https://doi.org/10.1029/2010PA002083

1132   DiNezio, P. N., & Tierney, J. E. (2013). The effect of sea level on glacial Indo-Pacific climate. *Nature Geoscience*,

1133   *6*(6), 485–491. https://doi.org/10.1038/ngeo1823

1134   DiNezio, P. N., Timmermann, A., Tierney, J. E., Jin, F., Otto-Bliesner, B., Rosenbloom, N., Mapes, B., Neale, R.,

1135   Ivanovic, R. F., & Montenegro, A. (2016). The climate response of the Indo-Pacific warm pool to glacial

1136   sea level. *Paleoceanography*, *31*(6), 866–894. https://doi.org/10.1002/2015PA002890

1137   Ding, Z. L., Derbyshire, E., Yang, S. L., Yu, Z. W., Xiong, S. F., & Liu, T. S. (2002). Stacked 2.6-Ma grain size

1138   record from the Chinese loess based on five sections and correlation with the deep-sea δ^{18}O record:

1139   STACKED QUATERNARY CLIMATE RECORD FROM CHINESE LOESS. *Paleoceanography*, *17*(3),

1140   5-1-5–21. https://doi.org/10.1029/2001PA000725

1141   Diz, P., & Pérez-Arlucea, M. (2021). Southern Ocean sourced waters modulate Eastern Equatorial Pacific

1142   denitrification during the Mid-Pleistocene transition. *Palaeogeography, Palaeoclimatology, Palaeoecology*,

1143   *577*, 110531. https://doi.org/10.1016/j.palaeo.2021.110531

1144   Du, X., Russell, J. M., Liu, Z., Otto-Bliesner, B. L., Gao, Y., Zhu, C., Oppo, D. W., Mohtadi, M., Yan, Y., Galy, V.

1145   V., & He, C. (2021). Deglacial trends in Indo-Pacific warm pool hydroclimate in an isotope-enabled Earth

1146   system model and implications for isotope-based paleoclimate reconstructions. *Quaternary Science*

1147   *Reviews*, *270*, 107188. https://doi.org/10.1016/j.quascirev.2021.107188

1148   Ehrenberg, S., & Svånå, T. A. (2001). Use of spectral gamma-ray signature to interpret stratigraphic surfaces in

1149   carbonate strata: An example from the Finnmark carbonate platform (Carboniferous-Permian). *Marine*

1150   *Pollution Bulletin*, *9*(3), 63. https://doi.org/10.1016/0025-326X(78)90448-4

1151   Eroglu, D., McRobie, F. H., Ozken, I., Stemler, T., Wyrwoll, K.-H., Breitenbach, S. F. M., Marwan, N., & Kurths, J.

1152   (2016). See–saw relationship of the Holocene East Asian–Australian summer monsoon. *Nature*

1153   *Communications*, *7*(1), 12929. https://doi.org/10.1038/ncomms12929

1154   Etourneau, J., Martinez, P., Blanz, T., & Schneider, R. (2009). Pliocene–Pleistocene variability of upwelling

1155   activity, productivity, and nutrient cycling in the Benguela region. *Geology*, *37*(10), 871–874.

1156   https://doi.org/10.1130/G25733A.1

1157   Etourneau, J., Robinson, R. S., Martinez, P., & Schneider, R. (2013). Equatorial Pacific peak in biological

1158   production regulated by nutrient and upwelling during the late Pliocene/early Pleistocene cooling.

1159   *Biogeosciences*, *10*(8), 5663–5670. https://doi.org/10.5194/bg-10-5663-2013

1160   Fang, X., An, Z., Clemens, S. C., Zan, J., Shi, Z., Yang, S., & Han, W. (2020). The 3.6-Ma aridity and westerlies

1161   history over midlatitude Asia linked with global climatic cooling. *Proceedings of the National Academy of*

1162   *Sciences*, *117*(40), 24729–24734. https://doi.org/10.1073/pnas.1922710117

1163   Fedorov, A. V., Burls, N. J., Lawrence, K. T., & Peterson, L. C. (2015). Tightly linked zonal and meridional sea

1164   surface temperature gradients over the past five million years. *Nature Geoscience*, *8*(12), 975–980.

1165   https://doi.org/10.1038/ngeo2577

1166   Feng, M., Zhang, N., Liu, Q., & Wijffels, S. (2018). The Indonesian throughflow, its variability and centennial

1167   change. *Geoscience Letters*, *5*(1), 3. https://doi.org/10.1186/s40562-018-0102-2

1168   Gallagher, S. J., Wallace, M. W., Li, C. L., Kinna, B., Bye, J. T., Akimoto, K., & Torii, M. (2009). Neogene history

1169   of the West Pacific Warm Pool, Kuroshio and Leeuwin currents: NEOGENE WEST PACIFIC WARM

1170   POOL. *Paleoceanography*, *24*(1), n/a-n/a. https://doi.org/10.1029/2008PA001660

1171   Geen, R., Bordoni, S., Battisti, D. S., & Hui, K. (2020). Monsoons, ITCZs, and the Concept of the Global Monsoon.

1172   *Reviews of Geophysics*, *58*(4). https://doi.org/10.1029/2020RG000700

1173   Gingele, F. X., & De Deckker, P. (2004). Fingerprinting Australia's rivers with clay minerals and the application for

1174   the marine record of climate change. *Australian Journal of Earth Sciences*, *51*(3), 339–348.

1175   https://doi.org/10.1111/j.1400-0952.2004.01061.x

1176   Gong, L., Holbourn, A., Kuhnt, W., Opdyke, B., Zhang, Y., Ravelo, A. C., Zhang, P., Xu, J., Matsuzaki, K., Aiello,

1177   I., Beil, S., & Andersen, N. (2023). Middle Pleistocene re-organization of Australian Monsoon. *Nature*

1178   *Communications*, *14*(1), 2002. https://doi.org/10.1038/s41467-023-37639-x

1179   Gordon, A. L., & Fine, R. A. (1996). Pathways of water between the Pacific and Indian oceans in the Indonesian

1180   seas. *Nature*, *379*(6561), 146–149. https://doi.org/10.1038/379146a0

1181   Gordon, A. L., Susanto, R. D., & Vranes, K. (2003). Cool Indonesian throughflow as a consequence of restricted

1182   surface layer flow. *Nature*, *425*(6960), 824–828. https://doi.org/10.1038/nature02038

1183   Hammer, Ø., Harper, D. A. T., & Ryan, P. D. (2001). *PAST: paleontological statistics software package for*

1184   *education and data analysis.* [Palaeontologia Electron. 4(1): 9 pp].

1185   Harris, P. G., Zhao, M., Rosell-Melé, A., Tiedemann, R., Sarnthein, M., & Maxwell, J. R. (1996). Chlorin

1186   accumulation rate as a proxy for Quaternary marine primary productivity. *Nature*, *383*(6595), 63–65.

1187   https://doi.org/10.1038/383063a0

1188   He, Y., Wang, H., & Liu, Z. (2021). Development of the Leeuwin Current on the northwest shelf of Australia

1189   through the Pliocene-Pleistocene period. *Earth and Planetary Science Letters*, *559*, 116767.

1190   https://doi.org/10.1016/j.epsl.2021.116767

1191   Heidemann, H., Cowan, T., Henley, B. J., Ribbe, J., Freund, M., & Power, S. (2023). Variability and long-term

1192   change in Australian monsoon rainfall: A review. *WIREs Climate Change*. https://doi.org/10.1002/wcc.823

1193   Herbert, T. D., Peterson, L. C., Lawrence, K. T., & Liu, Z. (2010). Tropical Ocean Temperatures Over the Past 3.5

1194   Million Years. *Science*, *328*(5985), 1530–1534. https://doi.org/10.1126/science.1185435

1195   Holbourn, A., Kuhnt, W., Kawamura, H., Jian, Z., Grootes, P., Erlenkeuser, H., & Xu, J. (2005). Orbitally paced

1196   paleoproductivity variations in the Timor Sea and Indonesian Throughflow variability during the last 460

1197   kyr: TIMOR SEA PALEOPRODUCTIVITY. *Paleoceanography*, *20*(3), n/a-n/a.

1198   https://doi.org/10.1029/2004PA001094

1199   Hollstein, M., Mohtadi, M., Rosenthal, Y., Prange, M., Oppo, D. W., Martínez Méndez, G., Tachikawa, K., Moffa

1200   Sanchez, P., Steinke, S., & Hebbeln, D. (2018). Variations in Western Pacific Warm Pool surface and

1201   thermocline conditions over the past 110,000 years: Forcing mechanisms and implications for the glacial

1202   Walker circulation. *Quaternary Science Reviews*, *201*, 429–445.

1203   https://doi.org/10.1016/j.quascirev.2018.10.030

1204   Hopmans, E. C., Weijers, J. W. H., Schefuß, E., Herfort, L., Sinninghe Damsté, J. S., & Schouten, S. (2004). A

1205   novel proxy for terrestrial organic matter in sediments based on branched and isoprenoid tetraether lipids.

1206   *Earth and Planetary Science Letters*, *224*(1–2), 107–116. https://doi.org/10.1016/j.epsl.2004.05.012

1207 Ishiwa, T., Yokoyama, Y., Reuning, L., McHugh, C. M., De Vleeschouwer, D., & Gallagher, S. J. (2019).

1208   Australian Summer Monsoon variability in the past 14,000 years revealed by IODP Expedition 356

1209   sediments. *Progress in Earth and Planetary Science*, *6*(1), 17. https://doi.org/10.1186/s40645-019-0262-5

1210 Iwakiri, T., & Watanabe, M. (2019). Strengthening of the Indian Ocean Dipole With Increasing Seasonal Cycle in

1211   the Mid-Holocene. *Geophysical Research Letters*, *46*(14), 8320–8328.

1212   https://doi.org/10.1029/2019GL083088

1213 Jia, G., & Li, Z. (2011). Easterly denitrification signal and nitrogen fixation feedback documented in the western

1214   Pacific sediments: DENITRIFICATION RECORD IN WEST PACIFIC. *Geophysical Research Letters*,

1215   *38*(24), n/a-n/a. https://doi.org/10.1029/2011GL050021

1216 Jian, Z., Wang, Y., Dang, H., Mohtadi, M., Rosenthal, Y., Lea, D. W., Liu, Z., Jin, H., Ye, L., Kuhnt, W., & Wang,

1217   X. (2022). Warm pool ocean heat content regulates ocean–continent moisture transport. *Nature*, *612*(7938),

1218   92–99. https://doi.org/10.1038/s41586-022-05302-y

1219 Kaboth-Bahr, S., & Mudelsee, M. (2022). The multifaceted history of the Walker Circulation during the Plio-

1220   Pleistocene. *Quaternary Science Reviews*, *286*, 107529. https://doi.org/10.1016/j.quascirev.2022.107529

1221 Kershaw, P., Martin, H. A., & Mason, J. M. (2017). *History of the Australian Vegetation: Cretaceous to Recent* (R.

1222   S. Hill, Ed.; Reprint). University of Adelaide Press. https://doi.org/10.20851/australian-vegetation

1223 Kershaw, P., Moss, P., & Van Der Kaars, S. (2003a). Causes and consequences of long-term climatic variability on

1224   the Australian continent: *Long term climatic variability*. *Freshwater Biology*, *48*(7), 1274–1283.

1225   https://doi.org/10.1046/j.1365-2427.2003.01085.x

1226 Kershaw, P., van der Kaars, S., & Moss, P. T. (2003b). Late Quaternary Milankovitch-scale climatic change and

1227   variability and its impact on monsoonal Australasia. *Marine Geology*, *201*(1–3), 81–95.

1228   https://doi.org/10.1016/S0025-3227(03)00210-X

1229 Klinkhammer, G. P., & Palmer, M. R. (1991). Uranium in the oceans: Where it goes and why. *Geochimica et*

1230   *Cosmochimica Acta*, *55*(7), 1799–1806. https://doi.org/10.1016/0016-7037(91)90024-Y

1231 Kong, T., Wang, Y., Sigman, D., Ren, H., & Wang, X. (2021). *Revisiting glacial-interglacial changes in pelagic*

1232   *denitrification in the South Pacific*. *2021*, PP34B-10.

1233 Kotov, S., & Pälike, H. (2018). *QAnalySeries – a cross-platform time series tuning and analysis tool* [Other].

1234   Geology. https://doi.org/10.1002/essoar.10500226.1

1235   Kuhnt, W., Holbourn, A., Hall, R., Zuvela, M., & Käse, R. (2004). Neogene history of the Indonesian Throughflow.

1236   In P. Clift, W. Kuhnt, P. Wang, & D. Hayes (Eds.), *Geophysical Monograph Series* (Vol. 149, pp. 299–

1237   320). American Geophysical Union. https://doi.org/10.1029/149GM16

1238   Kuhnt, W., Holbourn, A., Xu, J., Opdyke, B., De Deckker, P., Röhl, U., & Mudelsee, M. (2015). Southern

1239   Hemisphere control on Australian monsoon variability during the late deglaciation and Holocene. *Nature*

1240   *Communications*, *6*(1), 5916. https://doi.org/10.1038/ncomms6916

1241   Lacerra, M., Sigman, D., Martinez-Garcia, A., & Haug, G. (2021). *A foraminifera-bound nitrogen isotope record*

1242   *from the eastern tropical North Pacific spanning the last glacial-interglacial transition*. *2021*, PP41A-03.

1243   Lambert, J. E., Gibson, K. A., Linsley, B. K., Bova, S. C., Rosenthal, Y., & Surprenant, M. (2022). Equatorial

1244   Pacific bulk sediment $\delta^{15}N$ supports a secular increase in Southern Ocean nitrate utilization after the mid-

1245   Pleistocene Transition. *Quaternary Science Reviews*, *278*, 107348.

1246   https://doi.org/10.1016/j.quascirev.2021.107348

1247   Lawrence, K. T., Liu, Z., & Herbert, T. D. (2006). Evolution of the Eastern Tropical Pacific Through Plio-

1248   Pleistocene Glaciation. *Science*, *312*(5770), 79–83. https://doi.org/10.1126/science.1120395

1249   Li, L., Li, Q., Tian, J., Wang, P., Wang, H., & Liu, Z. (2011). A 4-Ma record of thermal evolution in the tropical

1250   western Pacific and its implications on climate change. *Earth and Planetary Science Letters*, *309*(1–2), 10–

1251   20. https://doi.org/10.1016/j.epsl.2011.04.016

1252   Lisiecki, L. E., & Raymo, M. E. (2005). A Pliocene-Pleistocene stack of 57 globally distributed benthic $\delta^{18}O$

1253   records: PLIOCENE-PLEISTOCENE BENTHIC STACK. *Paleoceanography*, *20*(1), n/a-n/a.

1254   https://doi.org/10.1029/2004PA001071

1255   Liu, Y., Lo, L., Shi, Z., Wei, K.-Y., Chou, C.-J., Chen, Y.-C., Chuang, C.-K., Wu, C.-C., Mii, H.-S., Peng, Z.,

1256   Amakawa, H., Burr, G. S., Lee, S.-Y., DeLong, K. L., Elderfield, H., & Shen, C.-C. (2015). Obliquity

1257   pacing of the western Pacific Intertropical Convergence Zone over the past 282,000 years. *Nature*

1258   *Communications*, *6*(1), 10018. https://doi.org/10.1038/ncomms10018

1259   Liu, Z., Altabet, M. A., & Herbert, T. D. (2005). Glacial-interglacial modulation of eastern tropical North Pacific

1260   denitrification over the last 1.8-Myr. *Geophysical Research Letters*, *32*(23), L23607.

1261   https://doi.org/10.1029/2005GL024439

Liu, Z., Altabet, M. A., & Herbert, T. D. (2008). Plio-Pleistocene denitrification in the eastern tropical North Pacific: Intensification at 2.1 Ma: ETNP DENITRIFICATION INTENSIFICATION AT 2.1 MA. *Geochemistry, Geophysics, Geosystems*, *9*(11), n/a-n/a. https://doi.org/10.1029/2008GC002044

Lo, L., Shen, C.-C., Zeeden, C., Tsai, Y.-H., Yin, Q., Yang, C.-C., Chang, T.-L., Su, Y.-C., Mii, H.-S., Chuang, C.-K., & Chen, Y.-C. (2022). Orbital control on the thermocline structure during the past 568 kyr in the Solomon Sea, southwest equatorial Pacific. *Quaternary Science Reviews*, *295*, 107756. https://doi.org/10.1016/j.quascirev.2022.107756

Lyle, M. W., Drury, Anna Joy, Tian, Jun, Wilkens, Roy H, & Westerhold, Thomas. (2019). *Table SM-14: ODP Site 138-849 spliced benthic foraminiferal stable isotope data* (p. 7171 data points) [Text/tab-separated-values]. PANGAEA. https://doi.org/10.1594/PANGAEA.904425

Martin, H. A. (2006). Cenozoic climatic change and the development of the arid vegetation in Australia. *Journal of Arid Environments*, *66*(3), 533–563. https://doi.org/10.1016/j.jaridenv.2006.01.009

Martin, H., & McMinn, A. (1994). Late Cainozoic Vegetation History of North-Western Australia, From the Palynology of a Deep Sea Core (ODP Site 765). *Australian Journal of Botany*, *42*(1), 95. https://doi.org/10.1071/BT9940095

Martínez-Garcia, A., Rosell-Melé, A., Jaccard, S. L., Geibert, W., Sigman, D. M., & Haug, G. H. (2011). Southern Ocean dust–climate coupling over the past four million years. *Nature*, *476*(7360), 312–315. https://doi.org/10.1038/nature10310

Martínez-Garcia, A., Rosell-Melé, A., McClymont, E. L., Gersonde, R., & Haug, G. H. (2010). Subpolar Link to the Emergence of the Modern Equatorial Pacific Cold Tongue. *Science*, *328*(5985), 1550–1553. https://doi.org/10.1126/science.1184480

Martinez-Garcia, A., Rosell-Mele, A., McClymont, E. L., Gersonde, R., & Haug, G. H. (2010). Subpolar Link to the Emergence of the Modern Equatorial Pacific Cold Tongue. *Science*, *328*(5985), 1550–1553. https://doi.org/10.1126/science.1184480

McLaren, S., Wallace, M. W., & Reynolds, T. (2012). The Late Pleistocene evolution of palaeo megalake Bungunnia, southeastern Australia: A sedimentary record of fluctuating lake dynamics, climate change and the formation of the modern Murray River. *Palaeogeography, Palaeoclimatology, Palaeoecology*, *317–318*, 114–127. https://doi.org/10.1016/j.palaeo.2011.12.020

Meyers, P. A. (1994). Preservation of elemental and isotopic source identification of sedimentary organic matter. *Chemical Geology*, *114*(3–4), 289–302. https://doi.org/10.1016/0009-2541(94)90059-0

Michael W. Wara, Ana Christina Ravelo, & Margaret L. Delaney. (2005). Permanent El Nino-Like Conditions During the Pliocene Warm Period. *Science*, *309*(5735), 758–761. https://doi.org/10.1126/science.1112596

Mix, A. C., Pisias, Nicklas G, Rugh, W D, Wilson, June, Morey, Ann E, & Hagelberg, Teresa King. (1995). *Final stable oxygen and carbon isotope ratios of benthic foraminifera versus age of ODP Site 138-849 on the East Pacific Rise* (p. 4245 data points) [Text/tab-separated-values]. PANGAEA. https://doi.org/10.1594/PANGAEA.60261

Müller, A., & Opdyke, B. N. (2000). Glacial-interglacial changes in nutrient utilization and paleoproductivity in the Indonesian Throughflow sensitive Timor Trough, easternmost Indian Ocean. *Paleoceanography*, *15*(1), 85–94. https://doi.org/10.1029/1999PA900046

Müller, P. J., Kirst, G., Ruhland, G., Von Storch, I., & Rosell-Melé, A. (1998). Calibration of the alkenone paleotemperature index U37K′ based on core-tops from the eastern South Atlantic and the global ocean (60°N-60°S). *Geochimica et Cosmochimica Acta*, *62*(10), 1757–1772. https://doi.org/10.1016/S0016-7037(98)00097-0

Paillard, D., Labeyrie, L., & Yiou, P. (1996). Macintosh Program performs time-series analysis. *Eos, Transactions American Geophysical Union*, *77*(39), 379–379. https://doi.org/10.1029/96EO00259

Peterson, L. C., Lawrence, K. T., Herbert, T. D., Caballero-Gill, R., Wilson, J., Huska, K., Miller, H., Kelly, C., Seidenstein, J., Hovey, D., & Holte, L. (2020). Plio-Pleistocene Hemispheric (A)Symmetries in the Northern and Southern Hemisphere Midlatitudes. *Paleoceanography and Paleoclimatology*, *35*(3). https://doi.org/10.1029/2019PA003720

Petrick, B., Martínez-García, A., Auer, G., Reuning, L., Auderset, A., Deik, H., Takayanagi, H., De Vleeschouwer, D., Iryu, Y., & Haug, G. H. (2019). Glacial Indonesian Throughflow weakening across the Mid-Pleistocene Climatic Transition. *Scientific Reports*, *9*(1), 16995. https://doi.org/10.1038/s41598-019-53382-0

Pisias, N. G., & Moore, T. C. (1981). The evolution of Pleistocene climate: A time series approach. Earth and Planetary Science Letters, 52(2), 450–458. https://doi.org/10.1016/0012-821X(81)90197-7

Prahl, F. G., & Wakeham, S. G. (1987). Calibration of unsaturation patterns in long-chain ketone compositions for palaeotemperature assessment. *Nature*, *330*(6146), 367–369. https://doi.org/10.1038/330367a0

1318   Rafter, P. A., & Charles, C. D. (2012). Pleistocene equatorial Pacific dynamics inferred from the zonal asymmetry in

1319   sedimentary nitrogen isotopes: CURRENTS. *Paleoceanography*, *27*(3), n/a-n/a.

1320   https://doi.org/10.1029/2012PA002367

1321   Ravelo, A. C., Andreasen, D. H., Lyle, M., Olivarez Lyle, A., & Wara, M. W. (2004). Regional climate shifts caused

1322   by gradual global cooling in the Pliocene epoch. *Nature*, *429*(6989), 263–267.

1323   https://doi.org/10.1038/nature02567

1324   Ravelo, A. C., Simonne Dekens, P., & McCarthy, M. (2006). Evidence for El Niño–like conditions during the

1325   Pliocene. *GSA Today*, *16*(3), 4. https://doi.org/10.1130/1052-5173(2006)016<4:EFENLC>2.0.CO;2

1326   Rein, B., & Sirocko, F. (2002). In-situ reflectance spectroscopy—Analysing techniques for high-resolution pigment

1327   logging in sediment cores. *International Journal of Earth Sciences*, *91*(5), 950–954.

1328   https://doi.org/10.1007/s00531-002-0264-0

1329   Rohling, E. J., Foster, G. L., Grant, K. M., Marino, G., Roberts, A. P., Tamisiea, M. E., & Williams, F. (2014). Sea-

1330   level and deep-sea-temperature variability over the past 5.3 million years. *Nature*, *508*(7497), 477–482.

1331   https://doi.org/10.1038/nature13230

1332   Rosenthal, Y., Holbourn, A. E., Kulhanek, D. K., & Expedition 363 Scientists. (2017). *International Ocean*

1333   *Discovery Program Expedition 363 Preliminary Report Western Pacific Warm Pool Neogene and*

1334   *Quaternary records of Western Pacific Warm Pool paleoceanography*. International Ocean Discovery

1335   Program. https://doi.org/10.14379/iodp.pr.363.2017

1336   Rosenthal, Y., Holbourn, A. E., Kulhanek, D. K., & Expedition 363 Scientists (Eds.). (2018). *Western Pacific Warm*

1337   *Pool* (Vol. 363). International Ocean Discovery Program. https://doi.org/10.14379/iodp.proc.363.2018

1338   Rousselle, G., Beltran, C., Sicre, M.-A., Raffi, I., & De Rafélis, M. (2013). Changes in sea-surface conditions in the

1339   Equatorial Pacific during the middle Miocene–Pliocene as inferred from coccolith geochemistry. *Earth and*

1340   *Planetary Science Letters*, *361*, 412–421. https://doi.org/10.1016/j.epsl.2012.11.003

1341   Schlitzer, R. (2023). *Ocean Data View*. odv.awi.de, 2023

1342   Schouten, S., Hopmans, E. C., Schefuß, E., & Sinninghe Damsté, J. S. (2002). Distributional variations in marine

1343   crenarchaeotal membrane lipids: A new tool for reconstructing ancient sea water temperatures? *Earth and*

1344   *Planetary Science Letters*, *204*(1–2), 265–274. https://doi.org/10.1016/S0012-821X(02)00979-2

1345 Singarayer, J. S., Valdes, P. J., & Roberts, W. H. G. (2017). Ocean dominated expansion and contraction of the late

1346   Quaternary tropical rainbelt. *Scientific Reports*, *7*(1), 9382. https://doi.org/10.1038/s41598-017-09816-8

1347 Smith, R. A., Castañeda, I. S., Groeneveld, J., De Vleeschouwer, D., Henderiks, J., Christensen, B. A., Renema, W.,

1348   Auer, G., Bogus, K. A., Gallagher, S. J., & Fulthorpe, C. (2020). *Indonesian Throughflow and Leeuwin*

1349   *Current dynamics in the Plio-Pleistocene. 2020*, PP037-0005.

1350 Stuut, J. W., De Deckker, P., Saavedra-Pellitero, M., Bassinot, F., Drury, A. J., Walczak, M. H., Nagashima, K., &

1351   Murayama, M. (2019). A 5.3-Million-Year History of Monsoonal Precipitation in Northwestern Australia.

1352   *Geophysical Research Letters*, *46*(12), 6946–6954. https://doi.org/10.1029/2019GL083035

1353 Stuut, J.-B. W., Temmesfeld, F., & De Deckker, P. (2014). A 550 ka record of aeolian activity near North West

1354   Cape, Australia: Inferences from grain-size distributions and bulk chemistry of SE Indian Ocean deep-sea

1355   sediments. *Quaternary Science Reviews*, *83*, 83–94. https://doi.org/10.1016/j.quascirev.2013.11.003

1356 Sun, Y., Clemens, S. C., An, Z., & Yu, Z. (2006). Astronomical timescale and palaeoclimatic implication of stacked

1357   3.6-Myr monsoon records from the Chinese Loess Plateau. *Quaternary Science Reviews*, *25*(1–2), 33–48.

1358   https://doi.org/10.1016/j.quascirev.2005.07.005

1359 Sun, Y., Yin, Q., Crucifix, M., Clemens, S. C., Araya-Melo, P., Liu, W., Qiang, X., Liu, Q., Zhao, H., Liang, L.,

1360   Chen, H., Li, Y., Zhang, L., Dong, G., Li, M., Zhou, W., Berger, A., & An, Z. (2019). Diverse

1361   manifestations of the mid-Pleistocene climate transition. *Nature Communications*, *10*(1), 352.

1362   https://doi.org/10.1038/s41467-018-08257-9

1363 Suppiah, R. (1992). The Australian summer monsoon: A review. *Progress in Physical Geography: Earth and*

1364   *Environment*, *16*(3), 283–318. https://doi.org/10.1177/030913339201600302

1365 Susanto, R. D., Gordon, A. L., & Zheng, Q. (2001). Upwelling along the coasts of Java and Sumatra and its relation

1366   to ENSO. *Geophysical Research Letters*, *28*(8), 1599–1602. https://doi.org/10.1029/2000GL011844

1367 Talley, L. D., & Sprintall, J. (2005). Deep expression of the Indonesian Throughflow: Indonesian Intermediate

1368   Water in the South Equatorial Current. *Journal of Geophysical Research*, *110*(C10), C10009.

1369   https://doi.org/10.1029/2004JC002826

1370 Tomczak, M., & Godfrey, J. S. (1994). *Regional oceanography: An introduction* (1st ed). Pergamon.

1371 Tomczak, M., & Godfrey, J. S. (2003). *Regional oceanography: An introduction* (2. ed). Daya Publ. House.

1372   Wang, P., Clemens, S., Beaufort, L., Braconnot, P., Ganssen, G., Jian, Z., Kershaw, P., & Sarnthein, M. (2005).

1373   Evolution and variability of the Asian monsoon system: State of the art and outstanding issues. *Quaternary*

1374   *Science Reviews*, *24*(5–6), 595–629. https://doi.org/10.1016/j.quascirev.2004.10.002

1375   Wang, P., Tian, J., & Lourens, L. J. (2010). Obscuring of long eccentricity cyclicity in Pleistocene oceanic carbon

1376   isotope records. *Earth and Planetary Science Letters*, *290*(3–4), 319–330.

1377   https://doi.org/10.1016/j.epsl.2009.12.028

1378   White, S. M., & Ravelo, A. C. (2020). The Benthic B/Ca Record at Site 806: New Constraints on the Temperature

1379   of the West Pacific Warm Pool and the "El Padre" State in the Pliocene. *Paleoceanography and*

1380   *Paleoclimatology*, *35*(10). https://doi.org/10.1029/2019PA003812

1381   Xin, S., Shen, J., Zhang, W., Sun, W., & Xiao, X. (2020). East Asian winter monsoon evolution since the late

1382   Pliocene based on a pollen record from Lake Xingkai, northeast Asia. Quaternary Research, 93, 40–59.

1383   https://doi.org/10.1017/qua.2019.45

1384   Zhang, P., Xu, J., Holbourn, A., Kuhnt, W., Beil, S., Li, T., Xiong, Z., Dang, H., Yan, H., Pei, R., Ran, Y., & Wu,

1385   H. (2020). Indo-Pacific Hydroclimate in Response to Changes of the Intertropical Convergence Zone:

1386   Discrepancy on Precession and Obliquity Bands Over the Last 410 kyr. *Journal of Geophysical Research:*

1387   *Atmospheres*, *125*(14). https://doi.org/10.1029/2019JD032125

1388